New vuggy porosity models-based interpretation methodology for reliable pore system characterization, Ordovician carbonate reservoirs in Tahe Oilfield, North Tarim Basin

Issoufou Aboubacar Mahaman Salifou [a,b,*], Heng Zhang [a,b], Issoufou Ousmane Boukari [c], Moussa Harouna [c], Zhongxian Cai [a,b]

[a] *Key Laboratory of Tectonics and Petroleum Resources, Ministry of Education, China University of Geosciences, Wuhan, 430074, China*
[b] *School of Earth Resources, China University of Geosciences, Wuhan 430074, China. No. 388 Lumo Road, Hongshan District, Wuhan, Hubei Province, 430074, PR China*
[c] *Université Abdou Moumouni, Faculté des Sciences et Techniques, Département de Géologie, BP, 10662, Niamey, Niger*

ABSTRACT

Carbonate rocks are in general complex and commonly contain compound pore systems that can significantly affect the variations of physical properties; their petrophysical evaluation remains challenging, and the results are often uncertain.

This paper presents a new approach developed to establish vuggy porosity models that can be applied to successfully estimate vuggy porosity, both connected and separate vug fraction. It involves mainly partitioning the total porosity into fractions of its basic components, such as fractures, matrix porosity, and vugs. To estimate and decompose the total porosity, wireline methods involving standard porosity and borehole electrical image logs are integrated based on rock-physics modeling and image analysis techniques through a series of steps, which specifically have particular set of procedures performed rigorously to obtain accurate results. The determined fractions of the total-vug and separate-vug porosities are related to acoustic parameters to establish total-vug and separate-vug porosity models, respectively. Core analysis and thin-section-derived optical porosity (PHIO) are used to verify the log-derived porosities and validate the newly-established total porosity partition procedure.

The newly proposed vuggy porosity models yield optimal estimates that significantly match the measured quantities. They also show statistically better prediction accuracy, compared with previous models in literature, especially typical Lucia vug porosity models. In addition, the results indicate that the density log, which its combination to sonic and resistivity logs can enable separate-vug porosity calculation, is a good-total porosity estimator at least in low-touching vug zones. Together, this has proven the effectiveness of the present approach for porosity partitioning in carbonate rocks, and the vuggy porosity models derived could therefore be applied to other similar carbonate reservoir studies.

1. Introduction

Carbonate rocks are commonly complex and characterized by various reservoir space types such as, primary and dissolution inter- and intra-particle pores, fractures, moldic, and vugs. This diversity of pore space generally results in heterogeneous reservoirs with great variation in physical properties, and consequently causing immense technical difficulties and low hydrocarbon recovery in producing carbonate reservoirs, compared with sand-shale reservoirs (e.g. Winn, 1957; Smith et al., 2003; Farooq et al., 2019; Ding et al., 2020 Song et al., 2020). The diversity of the pore space characteristics in carbonates originates from the combined implications of non-homogeneous depositional rock-fabric facies and varied post-depositional diagenetic processes, such as compaction, dissolution, dolomitization, and karstification, and local/regional structural deformation, including stylolitization, and fracturing-faulting (Akbar et al., 1995; Perrin et al., 2007; Bahrami et al., 2017). Generally, these post-depositional processes result in significant

---

Nomenclature

A	applied equation according to the intercept-case and scenario (Table 2)
A_1, A_2, A_3	constants related to the fracture type, Eq. (A.7a) and Table A3
A_g	pixel amount of the gaps related to tool's arms, px
A_t	total pixel amount for 1 m length of FMI image sample, px
A_v	pixel amount assigned to vugs over 1 m length of FMI image sample, px
AC	acoustic log
API	American Petroleum Institute
C	acoustic intercept defined for total vug porosity modeling, μs/ft
C'	acoustic intercept defined for separate-vug porosity modeling, μs/ft
CGR	computed gamma ray, API
CNL	Compensated Neutron Log
D	departure magnitude between measured to predicted vug fraction at specific depth for a given model, fraction
DEN	density log; Compensated Formation Density Log (FDC)
D_f	formation depth, m
FMI	Formation MicroImager log
F-PHID	filtered density porosity, fraction
F-PHISUM	filtered sum total porosity, fraction
GR	gamma ray log
I	acoustic intercept equation according to a given case (Table 2)
I_{GR}	gamma ray index
K	empirical constant relating the mud resistivity to its density
MD	measured depth, m and ft
MD	mean departure magnitude between measured to predicted vug fraction at specific depth for a given model, fraction
MR	mean ratio of measured to predicted vug fraction for a given model
N	number of micrograph per thin-section
P	optical porosity related to a given micrograph, fraction
P'	weighted optical porosity related to a given thin-section image, fraction
PHIB	bulk porosity, fraction
PHICV	connected vug porosity, fraction
PHID	density porosity, fraction
PHIE	effective porosity, fraction
PHIF	fracture porosity obtained from resistivity logs, fraction
PHIF-FMI	fracture porosity interpreted from FMI image log, fraction
PHIN	neutron porosity, fraction
PHIND	neutron-density porosity, fraction
PHIO	optical porosity derived from thin-section image, fraction
PHIS	sonic porosity, fraction
PHISUM	sum total porosity, fraction
PHISV	separate-vug porosity, fraction
$PHISV\mu$	micro-moldic separate-vug porosity, fraction
PHIV	total vug porosity, fraction
PHIV$_{im}$	vug porosity interpreted from FMI log, fraction
R	ratio of measured to predicted vug fraction for a given model

R^2	coefficient of determination
R_D	deep resistivity from deep Laterolog (LLD), Ω.m
R_m	mud resistivity at formation temperature, Ω.m
R_{mf}	mud-filtrate resistivity at formation temperature, Ω.m
R_S	shallow resistivity from shallow Laterolog (LLS), Ω.m
$RMSE$	root mean square error
S	scenario (Table 2)
s	pore shape factor defined for total vug porosity modeling
s'	pore shape factor defined for separate-vug porosity modeling
T_f	formation temperature, °C
T_s	surface temperature, °C
V	compressional velocity
V_i	computed volume fraction of a mineral component, fraction
V_{ni}	normalized volume fraction of a mineral component, fraction
V_{sh}	shale volume, %
V_{Pfluid}	compressional velocity of fluid, km/sec
V_{Plog}	rock bulk compressional velocity, km/sec
$V_{Pmatrix}$	compressional velocity of rock matrix, km/sec
X_{Hi}	theoretical log response of a given mineral
X_{Mi}	pixel amount assigned to be porous in a micrograph, px
X_T	true matrix property; CNLMAT, DMAT and TMAT for true matrix neutron, density and slowness, respectively
Y	fracture discriminating index
Y_{Mi}	total pixel amount in a given micrograph, px
Δt	acoustic interval transit time, μs/ft
Δt_f	interval transit time of fluid, μs/ft
Δt_l	bulk or log-recorded interval transit time, μs/ft
Δt_{ma}	matrix interval transit time, μs/ft
ΔT	geothermal gradient, °C/km
φ	porosity or total porosity as in Eqs. (6) and (8a)
ρ	density, g/cm^3
ρ_f	fluid density, g/cm^3
ρ_b	bulk density, g/cm^3
ρ_m	mud density, g/cm^3
ρ_{ma}	matrix density, g/cm^3

Subscripts

b	bulk
cv	connected vug
D	density
f	fluid, formation, fracture
i	ith mineral component as in Eq. (A.1a) through Eq. (A.1c) or ith micrograph as in Eq. (7a) through Eq. (7c)
im	image
l	log
m	matrix, mud
ma	matrix
N	neutron, number of micrographs
P	primary velocity
S	surface, scenario
sv	separate vug
v	vug
T	true
μ	microporosity

primary porosity reduction and secondary porosity development as well as heterogeneous and multimodal pore-size distribution (Baqués et al., 2020). Typically, the pore size may range from nanometer (Nm) to cave-sized scales (Lucia, 2007; Nair et al., 2008; Ukar et al., 2020). Thus, to better understand carbonate pore systems and achieve reliable

porosity quantification, it is necessary to perform integrated studies using multi-scale data.

Many studies have been conducted using rock-physics models (Wyllie et al., 1956; Kuster and Toksöz, 1974; Anselmetti and Eberli, 1999; Sun, 2000; Saleh and Castagna, 2004) and digital rock image

analysis (Newberry et al., 1996; Anselmetti et al., 1998; Weger et al., 2009; Voorn et al., 2015; Fu et al., 2016; Ramandi et al., 2017; Buono et al., 2019; Hassan et al., 2019) to investigate carbonate pore type heterogeneity and understand its influence on the variations of reservoir physical properties (Sun, 2004; Sayers, 2008; Xu and Payne, 2009; Li and Zhang, 2018).

This study presents a new approach for determining and partitioning total porosity into fractions of its different pore components and establishing vuggy porosity models based on rock-physics modeling and image analysis in naturally fractured vuggy reservoirs. This can ensure reliable pore system characterization and successful reservoir evaluation. The different porosity fractions are determined from joint inversion of the standard porosity logs and processing of borehole electrical image log. After the detailed partition of the total porosity, the relative fractions of the total-vug and separate-vug porosities are plotted against multivariate acoustic transforms to develop the total-vug and separate-vug porosity models, respectively. The acoustic transforms are established from the modification of the acoustic model of Wyllie et al. (1956) and the generalized Wyllie acoustic model of Saleh and Castagna (2004). To verify the porosity interpretation results and ensure the reliability of the inputs for vuggy porosity modeling, we compare the log-derived total and effective porosity to the thin-section optical porosity (PHIO) and corrected full-diameter core porosity, respectively. The accuracy of the vuggy porosity modeling is further demonstrated through statistical analysis. Illustrations are given using data obtained from two key Wells (A and B) in the Tahe Oilfield, North Tarim Basin, China.

2. Previous works and research background

In literature, there are a plethora of studies on carbonate pore systems. In an attempt to sufficiently resolve the heterogeneity in carbonate pore structures, several authors have conducted integrated studies involving reservoir geology, geophysics, and petrophysics (e.g. Perrin et al., 2007; Clerke et al., 2008; Sajjad et al., 2016). Such studies usually ensure accurate prediction of spatial pore system distribution and understand its connections with reservoir physical properties (Ghadami et al., 2015; Inês et al., 2015). Anselmetti and Eberli (1999) applied the velocity deviation log concept to study pore type distribution and permeability variation. Ramakrishnan et al. (2001) and Yarmohammadi et al. (2020) have discussed a reservoir evaluation approach based on image processing, and analytical modeling of shear-modulus and transport properties to classify the rock-facies, partition pore system, and compute petrophysical properties, such as resistivity, and permeability. The method combines core and logging data, including core-thin sections, and standard nuclear, nuclear magnetic resonance (NMR), and borehole electrical image logs. Tyagi and Bhaduri (2002) and Cunningham et al. (2004) employed automatic image analysis and neural network methods to predict the reservoir facies and partition porosity to refining the characterization of a heterogeneous carbonate reservoir. Pérez-Rosales and Luna (2004) used empirical and theoretical models to investigate pore structure heterogeneity and numerically estimate the proportion of different pore components by exploiting the link between formation resistivity factor and porosity in naturally fractured vuggy reservoirs. Genty et al. (2007) classified the reservoir pore facies by quantifying some significantly related-geological attributes through a spectral decomposition of the NMR applying a Gaussian distribution and Bayesian framework combined to thin-section petrography. Weger et al. (2009) used a digital image analysis (DIA) method to determine pore geometrical parameters and assess their interconnections with reservoir physical properties such as velocity and permeability. Pirrone and Bona (2015) have attempted to characterize the reservoir pore systems and determine petrophysical properties, such as permeability, and fluid saturation, by integrating nuclear magnetic resonance (NMR) log, core-derived NMR data, mercury injection capillary pressure (MICP), and pressure, volume, and temperature (PVT) data. Rodolfo Soto et al. (2012) and Jonathan Soto et al. (2015) implemented a fuzzy logic

technique to classify the reservoir pore systems and derive reliable cementation factor data, which are necessary to ensure accurate reservoir petrophysical characterization. Sajjad et al. (2016) conducted reservoir quality evaluation using sequence stratigraphy and pore system classification. The approach consisted of investigating reservoir elastic, petrophysical, and dynamic properties. Bahrami et al. (2017) carried out reservoir quality evaluation through investigation of diagenesis-controlled pore facies distribution using core thin-section and well logging data. Wei et al. (2020) classified the pore systems using a modified NMR-based permeability model and description of thin-section and field emission scanning electron microscopic images in deeply buried microporous carbonates. Additionally, many studies were conducted based on X-ray computed tomography (CT) for effective pore system characterization, such as (i) analysis of reservoir petrophysical properties using the variations of pore types and net-confining stress as proxies (Wang et al., 2016) and (ii) automatic rock type classification relying the pore type characteristics (Li et al., 2017).

Based on the aforementioned and other relevant literature, a comprehensive characterization of pore structures in carbonate reservoirs requires developing an interpretation methodology. Such methodology should honor the integration of varied and independent data measured at different resolution throughout the entire pore-size scale range: μ-digital image data, core thin-section, logs, and seismic (Sun, 2000; Bayuk et al., 2019; Hassan et al., 2019; Ramamoorthy et al., 2019).

Practically, most difficulties encountered in evaluating carbonate porosity are related to the quantification of secondary porosity, particularly vugs. In this regard, a myriad of approaches has been developed based on acoustic modeling, and high-resolution image analysis using the standard sonic log, and borehole micro-resistivity image and ultrasonic borehole image, respectively (Ramakrishnan et al., 2001; Zohreh et al., 2016). The basis for such acoustic modeling arises from the strong dependence of physical properties, in the instance of velocity, on the pore structure types (Sun, 2004; Xu and Payne, 2009; Dou et al., 2011). For instance, for a given porosity, an acoustic velocity difference of 2.0 km/s or greater was reported owing to pore structure changes (Sun, 2004). Compared to relatively soft-rocks that contain predominantly inter-particle-and/or-crystalline and crack-like porous space, rocks containing frame-forming pore types (molds/vugs) which present high pore aspect ratio show much lower acoustic propagation time. These variations in the acoustic propagation time may result from the differential mechanical behavior, which can partly be associated with the change in the rock compressibility. Frame-forming pore types tend to decrease the rock compressibility in contrast to inter-particle-and/or-crystalline and crack-like porous space (Mavko and Mukerji, 1995; Saleh and Castagna, 2004; Sun et al., 2006; Weger et al., 2009; Wang et al., 2011).

Wyllie et al. (1956) laid the basics of porosity inversion from acoustic compressional velocity; the related acoustic model is called the Wyllie time-average equation (Wyllie et al., 1956). Subsequently, many methods and rock-physics models have been proposed to study pore type heterogeneity in carbonates, foremost of which are: (i) secondary porosity index (Schlumberger, 1974) (ii) pseudofluid transit time (Meese and Walther, 1967) (iii) Nurmi model (Nurmi, 1984) (iv) spherical inclusion model (Brie et al., 1985) (v) Lucia model (Lucia and Conti, 1987) (vi) quadratic- and power-law models (Wang and Lucia, 1993) (vii) velocity deviation concept (Anselmetti and Eberli, 1999) and (viii) generalized Wyllie's equation (Saleh and Castagna, 2004). Moreover, shear modulus-based acoustic modeling has also been applied to characterize carbonate pore structure, in particular, vug fraction estimation through an iterative process, as described by Ramamoorthy et al. (1999) and Ramakrishnan et al. (2001). Additionally, rock-frame properties based-acoustic models have been developed for pore type segmentation and heterogeneity analysis, and further, understand the variations of reservoir physical properties with the pore structure changes while taking into account the influence of the host-rock fabrics

(Sun, 2000; Huang et al., 2017; Jin et al., 2017; Li and Zhang, 2018). Recently, Mollajan and Memarian (2016) applied the Parzen classifier using elastic parameters to characterize the velocity-pore structure relationship and quantitatively identify the pore type composition through rock-physics modeling. However, though these models and approaches are somewhat applicable to investigate pore type heterogeneity in carbonate reservoirs, there are major concerns needing to be put into consideration for improved accuracy. For instance, the above models and approaches often apply the nuclear logs, density and neutron logs, or core analysis to determine the total porosity (a key input parameter), which may not be reliable; because sometimes poor recovery can be obtained at intervals with higher neutron-density porosity and vice versa, the hydrocarbon production rate may not necessarily correlate with the neutron-density total porosity. Additionally, it can also be observed that the available vuggy-porosity models mostly ignore the fracture porosity component, and they apply largely for separate-vug porosity estimation. It is because these models may have been developed based on field data related exclusively to separate-vugs bearing--reservoir formations.

Additionally, several attempts have been made to derive vug porosity and achieve reliable pore system characterization based on the transformation of borehole electrical image from the original resistivity map into a porosity map (e.g. Newberry et al., 1996; Ghafoori et al., 2009; Fu et al., 2016; Merza Media et al., 2019). The image interpretation can be conducted automatically and/or manually. Moreover, considering the applicability of the image analysis method in rock-physics studies, fast-growing digital technology has opened up reliable perspectives for carbonate reservoir studies. The method can enable to obtain statistical and geometrical measurements that are useful for qualitative pattern recognition and quantitative computation of rock physical properties (Anselmetti et al., 1998; Richa et al., 2006; Andrä et al., 2013; Voorn et al., 2015; Li et al., 2017; Hassan et al., 2019; Malik and Sharma, 2019; Mehmani et al., 2019).

3. Materials and methods

This study was conducted based on field data collected from sixteen Wells. A subset of sixth from the sixteen Wells considered in this investigation, including two key Wells A and B used for illustrations, have conventional logs, borehole electrical image logs, and core analysis data. The available suite of conventional well logs comprises the caliper (CAL), gamma-ray (GR), density (DEN), neutron (CNL), acoustic (AC), and deep and shallow resistivity (LLS and LLD) logs. A representative suite of samples was selected from the core database (82 core samples) for thin-section petrography and porosity determination at full-diameter (>10 cm) and plug scale. A total of 175 thin-sections prepared from blue-dyed epoxy resin impregnated core samples were observed using transmitted light microscopy. The epoxy was poured into dried samples under vacuum and high-pressure conditions. The digital thin-sections were acquired, and further, examined to compute optical porosity (PHIO) applying an image analysis technique. Additionally, the mud logging data were also used in the present investigation.

We conducted multi-mineral analysis to compute the rock volume mixture from combination of litho-porosity logs, such as AC, CNL, DEN, and GR logs, and subsequently establish the true matrix properties involved in the determination of the different porosities. The procedure applied is given in Appendix A.

Pore system composition was investigated to identify the basic pore type components through core visual inspection. Subsequently, the relative proportions of the identified basic pore types were then separately established and their relative sum was assumed to be a reasonable estimate of total porosity, which, is herein referred to as sum total porosity (PHISUM). Alternatively, the total porosity was estimated from Compensated Formation Density Log (FDC), and also by averaging the porosities derived from FDC log and Compensated Neutron Log (CNL). The matrix and fracture porosity were determined from the inversion of

the standard sonic log, and the combination of Dual Laterolog and Micro-resistivity logs, respectively. Additionally, sensitive log-response characteristics (AC and DEN logs) and borehole electrical image log were integrated to document the fracture system. It is suggested that the investigation of fractures as an independent pore type can allow a consistent quantitative pore system characterization. The fractions of vug porosities were determined by jointly interpreting the standard porosity and borehole electrical image logs. The electrical borehole and thin-section images were processed and analyzed using *Adobe Photoshop* and *Image-Pro Plus* software packages. The log-derived total and effective porosity were subsequently compared to the thin-section optical porosity (PHIO) and full-diameter core porosity, respectively; a further correction applied to the core effective porosity resulted in improved comparison.

After computing the rock volume mixture, determining the true matrix properties and having estimated the total porosity and portioned it into fractions of the identified pore types, such as interparticle or matrix porosity, fractures, and vugs (both connected and isolated), the relative fractions of the total-vug and separate-vug porosities were considered to establish the total-vug and separate-vug porosity models. The acoustic transforms involved in the vuggy porosity modeling were modified from the acoustic model of Wyllie et al. (1956) and the generalized Wyllie acoustic model of Saleh and Castagna (2004). The accuracy of the vuggy porosity modeling results was evaluated based on statistical analysis.

4. Results and discussion

4.1. Multi-mineral analysis

For many reasons, core analysis data may be missing, difficult to access for log analysts, or not available for the full reservoir depth-interval despite their critical significance (Salazar et al., 2008). Thus, to obtain the effective rock matrix properties necessary for accurate formation evaluation (e.g. porosity estimation, lithology definition), reservoir engineers very often rely on the inversion of a comprehensive well log suite. This approach enables successful computation of the rock matrix properties as well as the definition of high-resolution rock--formation types along with their changes in the reservoir depth (Serra and Abbott, 1982; Ijasan et al., 2013; Saneifar et al., 2015).

Herein, the litho-porosity borehole e-logs (i.e. GR, DEN, CNL, and AC logs) were combined to determine the true matrix properties using the FORWARD software package. The mineral model used is the limestone-dolomite-clays triad, and it was defined in accordance with the thin-section petrography and core analysis. For a modeling purpose, the interstitial formation fluid was assumed as fresh-water, though saline water and hydrocarbons are the actual formation fluids. The parameters defined to compute the rock volume mixture and the formulas applied to calculate the true matrix properties are given in Appendix A.

The rock volume composition can be computed to avoid the impact of the variations of the rock matrix lithology and successfully determine the effective rock matrix properties, which are useful for reliable porosity evaluation for continuous depth. The calculated rock properties were suggested as representative of the "true" properties because they depend strongly on the actual rock matrix properties and formation depth. Given that the resolution number obtained (~3.93) closely matches a "good" level of accuracy, the computation results are reasonably reliable.

4.2. Porosity determination using well logging methods

We investigated the pore system composition to identify the basic space types through visual core inspection. Fig. 1 shows typical core photographs. It demonstrates that the reservoir rocks are characterized by the presence of compound pore systems comprising any combination of the identified pore types, including inter- and intra-particle pores,
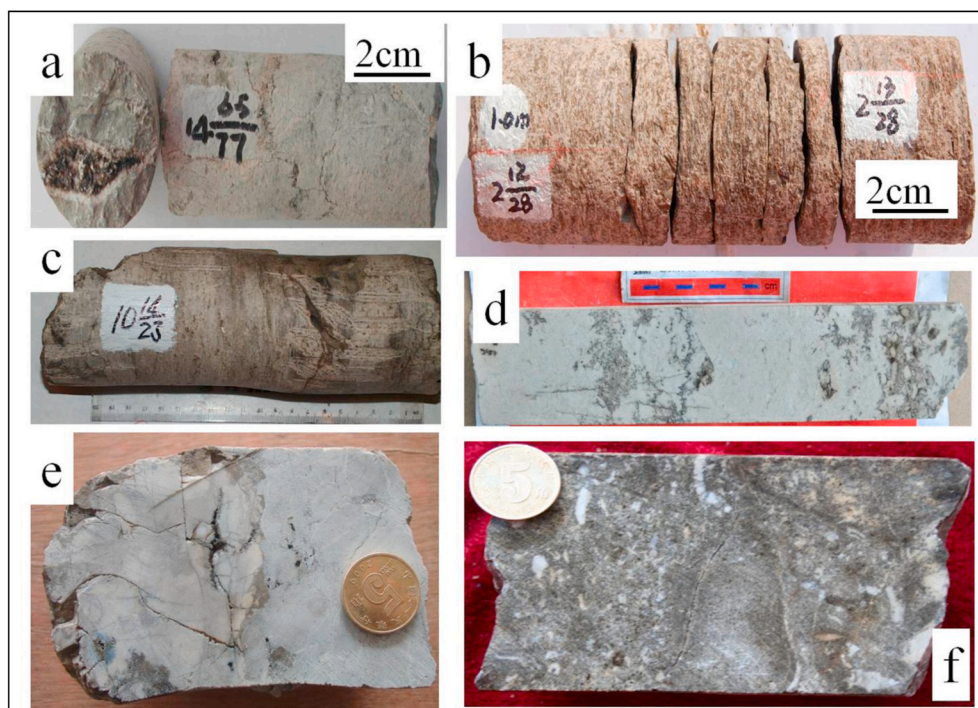
Fig. 1. Typical core photographs showing the reservoir pore types in the wells across the study formations. (a) Fractures, stylolites, filled-solution enlarged fracture, and vugs developed along fractures (Well B, 6005.15 m, O_2yj). (b) Parallel horizontal fractures with their surfaces covered by organic matter (Well E, 6127.26 m, $O_{1-2}y$). (c) Fractures, low-angle solution enlarged fracture, and vugs (Well A, 5855.1 m, O_1y). (d) Fractures, stylolites, and partially filled vugs (Well D, 5858.7 m, O_2yj). (e) Fissure-fracture networks, isolated vugs, and vugs developed along fractures (Well B, 6117.53 m, $O_{1-2}y$). (f) Primary interparticle and dissolution pores, and open and cemented fractures (Well C, 5956.7 m, O_2yj). The samples demonstrate the diversity and heterogeneity of the pore types. Note: top of core image is to the left for all samples.

fractures, and vugs. While taking into consideration the various aspects and features of the pore systems at large, the pore system description was conducted following several pore classification systems (Choquette and Pray, 1970; Lucia, 1983, 1995; Lønøy, 2006; Mousavi et al., 2012). For example, Lucia (1983, 1995) classified the carbonate pore space into matrix and vugs, which are further subdivided into separate vugs (molds, intra-fossil-grain, and shelter) and touching vugs (fractures, cavernous, breccias, and fenestral).

4.2.1. Estimation of density, neutron, neutron-density and sonic porosities

With the true matrix properties available, we calculated the density, neutron, neutron-density, and sonic porosities. The matrix or sonic porosity, and the neutron and density porosities were calculated using the Wyllie acoustic transform (Wyllie et al., 1956), and the model of Gaymard and Poupon (1968), respectively. The neutron-density porosity was determined as the average value of the neutron and density porosities. Accounting by the borehole conditions, the specificities of neutron and density measurements, and the petrophysical characteristics of the study formations, it was suggested that density log can provide a representative total porosity estimate, compared with the neutron log. The approach and formulas applied for these calculations are given in Appendix A.

4.2.2. Fracture porosity characterization

Fracture characterization has become critical for evaluating the reservoir performance because natural fractures, despite their relatively very low percentage in general, can significantly determine hydrocarbon production in reservoir rocks with low-to-tight porosity and extremely low permeability (Boyeldieu and Winchester, 1982; Deng et al., 2006; Xu and Payne, 2009; Ding et al., 2012; Xu et al., 2016). The fracture porosity was herein determined using the rock-physics model of Li et al. (1996), which combines the dual Laterolog−Microlog resistivity logs and, it has been demonstrated to be effective. The procedure applied is described in Appendix A. The results obtained show, in addition to the core investigation (Figs. 1 and 6), that the target formations are characterized by the occurrence of high to low angle horizontal and/or vertical parallel fractures, which contain secondary mineralization (clays, calcite, and organic compounds).

Furthermore, we evaluated the fracture porosity using highly sensitive log-response characteristics, such as AC and DEN logs. Comparing the sonic porosity and density porosity has allowed detecting the fractured intervals. These intervals are characterized by a relative increase and decrease in the bulk slowness and density, respectively, as well as, in the corresponding matrix properties depending on the fracture type, compared with non-fractured adjacent intervals. It is likely related to the loss of compaction providing the AC-energy loss pathway, and the presence of generally low-density materials, such as clays, and fluids, in fractured media. The fracture zones are identified as intervals showing a crossover between the sonic and density curves and abnormal variation of the log profiles. It is observed that: (1) opposite high-angle fractures, the density porosity is higher than the sonic porosity and their relative curves display an inverse C-shape and serrated (typical cycle skipping) profiles, respectively; (2) for low-angle fractures, the sonic porosity is higher than the density porosity and their curves display serrated and C-shape profiles, respectively; (3) intermediate-angle fractures, the density porosity is greater than the sonic porosity and the curves show relatively smooth trends (Xu et al., 2016). For non-fractured zones, the two porosity curves behave in a similar pattern or exhibit regularly parallel and unchanged trends with the density porosity constantly higher than the sonic porosity (Fig. 2). It suggests that the sonic porosity and density porosity may not reliably represent the actual matrix and total porosity, respectively, because of the contribution of fracture porosity opposite fractured reservoir interval.

The fracture detection ability is verified based on the full-borehole formation microresistivity image (FMI) log, which is believed to be a highly effective tool to characterize fractured media (e.g. Fowler et al., 1999; Barton and Zoback, 2002; Xu et al., 2016). The quantification of the fracture porosity from the FMI log follows the procedure, presented below, applied to determine the vuggy porosity. The values obtained agree with those interpreted from the standard resistivity logs, but agree much better in the upper section interval. In the lower section interval, the observed discrepancy is suggested related to the fact that the fractures are possibly small-scale fractures or micro-fractures (micro-cracks) and/or they likely contain very low conductivity materials, and thus they would not appear on the FMI log (Jacobsen et al., 1990). Additionally, the mismatch can be related to the presence of drilling-induced
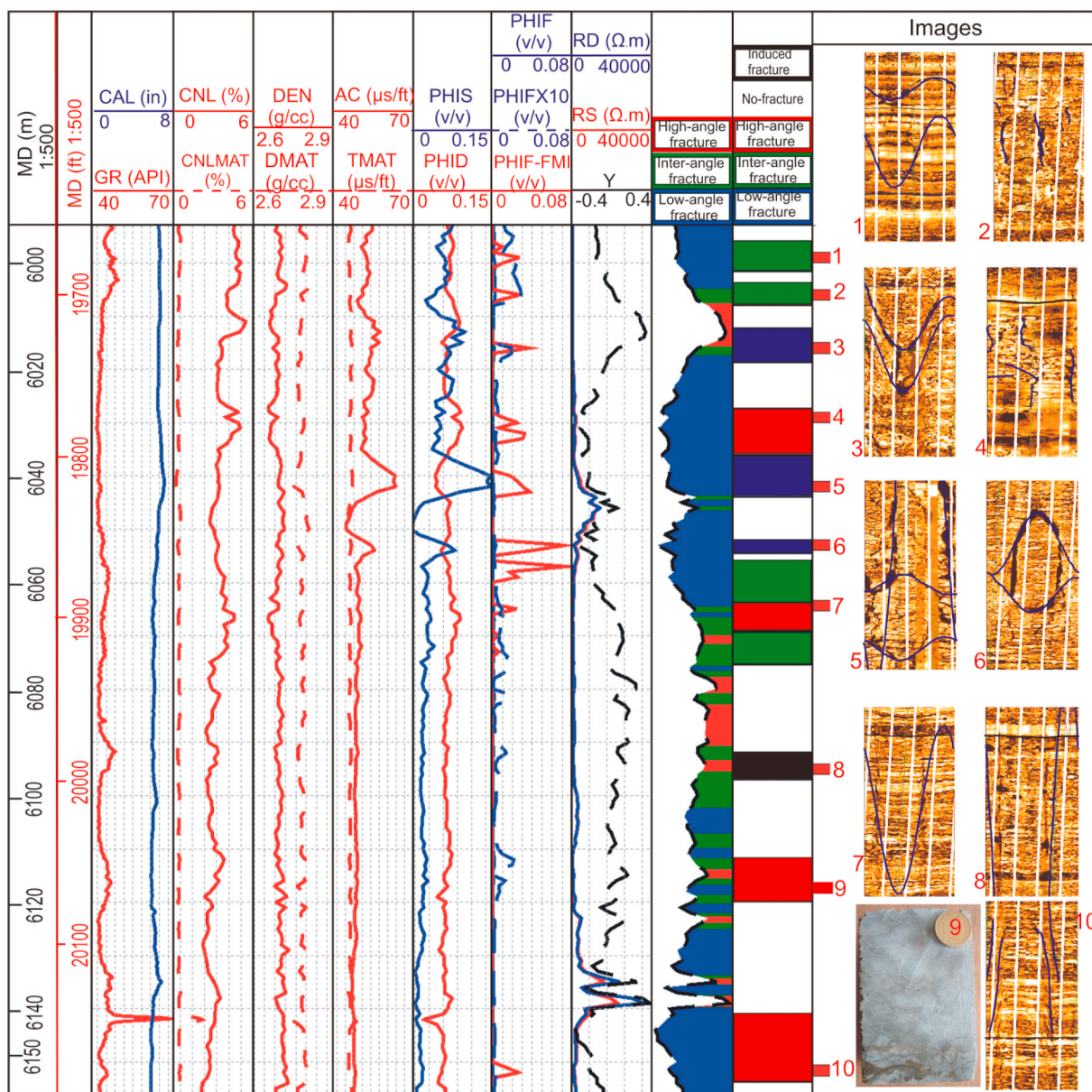
Fig. 2. The fracture-detection-classification-porosity calculation in the Well B. Left to right, the first track is the depth in meter; the second track is the depth in feet; the third is GR, CAL logs; the fourth is the bulk and matrix CNL logs; the fifth is the bulk and matrix DEN logs; the sixth is the bulk and matrix AC logs; the seventh is the AC and DEN porosity; the eighth is the resistivity log-derived fracture porosity (PHIF), PHIFx10, and FMI-derived fracture porosity (PHI-FMI); the ninth is the LLS-LLD logs and Y parameter; the tenth is the color display of the fracture type distribution according to the values of Y; the eleventh is the fracture type distribution from interpretation of sensitive logs (AC and DEN); and the twelfth is the dynamic FMI image samples (2 m length). The locations of images are indicated by the red rectangles with consistent numbering. The fracture zones can be identified at the density-sonic porosity crossover and abnormal variations. This was verified using the FMI image log from comparable depths. To enhance the comparison rate between the PHIF and PHIF-FMI, the PHIF values are multiplied by 10. (For interpretation of the references to color in this figure legend, the reader is referred to the Web version of this article.)

fractures (Fig. 2). The log-derived fracture porosity is multiplied by a factor of 10 to enhance its comparison with the image log-derived fracture porosity, and this resulted in an improved trend.

4.2.3. Vug-quantification from formation microresistivity image log

Lucia (1983, 1995) defined vugs as visible pore space within or significantly larger than the rock particles, grains, and crystals. For many carbonate reservoirs, vugs constitute a key pore type that can provide the main reservoir space, and they can significantly dominate the reservoir fluid conduction (Hurley et al., 1998; Saleh and Castagna, 2004). However, the identification and quantification of vugs pose immense technical challenges, and they become often likely impossible using (1-D) conventional wireline logs characterized by a coarser

resolution (Tyagi and Bhaduri, 2002). Therefore, it has become common practice to study vugs using appropriate tools such as borehole imagers that can provide continuous, azimuthally oriented, and high-resolution measurements at various scales. Such information has been increasingly exploited as a better way forward to work out the heterogeneity of carbonate pore systems by quantifying and determining the distribution of secondary pore types, particularly spherical and subspherical vugs and molds (e.g. Akbar et al., 1995; Hurley et al., 1998; Xu et al., 2006). Cases of FMI application-based studies include quantification of vuggy porosity (Delhomme, 1992), analysis of pore structure by investigating pore types heterogeneity and distribution (e.g. Newberry et al., 1996; Tilke et al., 2006; Xu et al., 2006), and characterization of carbonate microfacies and pore types (Meng et al., 2018).

The present approach for vug-quantification from the "dynamic" borehole microresistivity image followed somewhat the general workflow procedure for borehole image analysis but was modified to achieve the desired objective (Fig. 3a). The borehole electrical images were recorded using the MAXIS 500C, a Schlumberger's series of FMI logging tool. As usual, the FMI log was processed as a porosity map, where the dark inclusions can likely be vugs, to which a pixel-counting technique was applied using *Adobe Photoshop* software. The different steps are described successively in the following paragraphs.

1. The first step involved dividing the whole raw image log into a series of adjoining depth windows of similar size, in this case, 1 m length, and converting the image color system, in this case, the indexed to RGB color system (image representation). The image size redefinition and enhancement enable the improvement of the resolution to better distinguish the different features over each analysis depth window. The area of the image sample or total pixel amount (A_t) and that related to the gaps between tool 'arms and pads' (A_g) can be obtained automatically from the histogram panel. This step is a prerequisite in image segmentation.

2. The image segmentation procedure consisted to decompose the image into light and dark color containing-pixels. Though relatively simple, it requires great caution because of the complexity of carbonate rocks. A similarity detection-based approach, the threshold method, was applied to segment the image. First, a representative region, either light-colored or dark-colored, can be locally picked, and then selected throughout the image by applying the "Similar Selection" command. In this case, we used the dark-colored pixel region. Afterward, it was performed the "Layer Via Copy" command. A binary segmented image was obtained automatically with the background features being removed and showing only the dark-colored containing-pixels over a white background. The original image will also be available. Conventionally, the removed light-colored containing-pixels represent the resistive features (rock matrices), designated hereafter as noise. The dark-colored containing-pixels represent the conductive features, such as the bedding plane, low-resistivity massive structures, fractures, and dissolution pores (vugs, caverns, and karsts), which are subject to further analysis. This step paves the way for the upcoming steps.

3. Next, and just as important, over the binary image, the vug-containing-pixels were manually discriminated through a visual inspection and identification based on geometric criteria. This idea relies on the fact that geologic objects present some specificity in structural and textural patterns and attributes, though conductive features appear in dark color shades (Delhomme, 1992). For instance, vugs appear generally in an equant shape (circular to ellipsoidal) and are unconformable to adjacent host rock-fabric elements (Choquette and Pray, 1970). Fractures appear generally in thin and elongated shapes; the massive structures present mostly no specific regular shape (e.g. clay nodules), and the bedding interface is usually plane and thick (Chai et al., 2009).

4. Finally, having detected and isolated the desired feature "vug-related pixels", the counts of vugs-containing pixels (A_v) are directly obtained (in the histogram panel) by performing the "Local and Similar Selection" command. Importantly, the effects of fuzzy-contours (light reflection) and object-surrounding halos on the fraction of vugs-related pixels were automatically corrected by applying the edge detector filter. Thus, the vug fraction, referred to as image log-derived vuggy porosity (φ_{vim}) is determined as the ratio of A_v to the difference between A_t and A_g for an image sample. The accuracy of
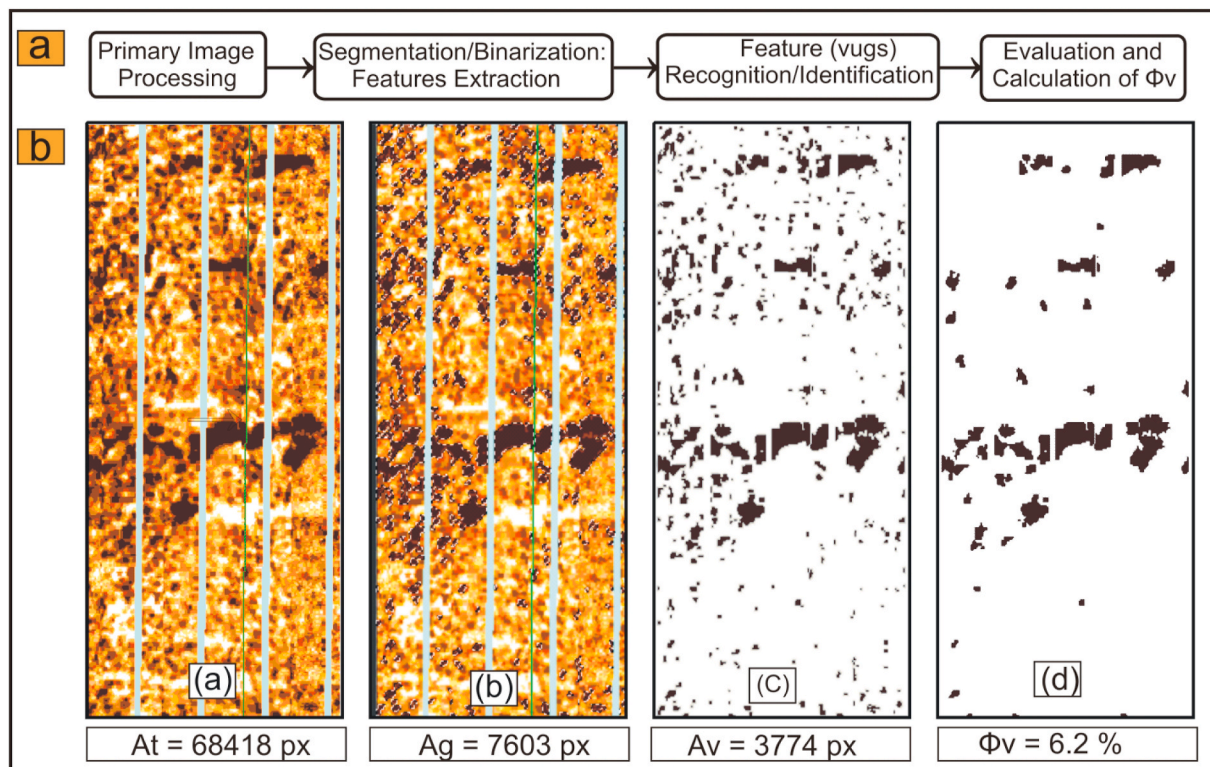
Fig. 3. (a) Workflow procedure. (b) Illustration of the vug extraction and quantification result using *Adobe Photoshop*. To start, the full image length is first divided into smaller 2D pieces of reasonable length, i.e.1 m length herein. It has to be mentioned the shorter the image length, the higher accuracy of the results obtained (Valentín et al., 2018). (a) Raw FMI image sample. (b) Delineation of conductive features. (c) Segmented image showing only the conductive features "dark-color pixels" over white background. (d) Processed segmented image displaying only the dark-colored pixels assigned to be vugs. A_t, A_g, and A_v are the total image pixel amount, cumulative gap pixel amount, and vug porosity fraction, respectively. Note: this is 1 m length image sample. (For interpretation of the references to color in this figure legend, the reader is referred to the Web version of this article.)

the values obtained is strongly dependent on, among others, the image quality (resolution) and the interpreter expertise because the procedure is not entirely automatic but rather, semi-automatic; thereby the efficiency of the approach may not somewhat meet the expectation. Fig. 3b schematically shows the illustration for the quantification of vugs from the FMI log.

Despite being computationally intensive (slow and time-consuming) and likely subjective, the present vug-quantification procedure enables one to accurately quantify the vug fraction (Valentín et al., 2018). In contrast to the automatic methods that apply some constraints to derive the porosity transform from the image log, it is not necessary for the present procedure. These methods assume that the borehole electrical image represents a 100% water-saturated flushed zone, and the image resistivity is somewhat equal to the shallow Laterolog resistivity,

LLS/SFLU (Newberry et al., 1996; Merza Media et al., 2019). Additionally, the significance of the procedure was demonstrated by calibrating the computed vug porosity-depth profile with some logging curves that present high correlation to the formation lithology and electric properties throughout the entire logged interval: high vug fraction tally with low RLLS and RLLD readings, and high computed GR (CGR, total GR discounted of uranium contribution) values, respectively, for comparable depth; the reverse is also verified (Fig. 4a and b). This can show that the quantified dark-colored pixels relate essentially to the vugs rather clays or other conductive minerals present, which can validate the quantification procedure and the results obtained. But, it should also be remembered that the formation resistivity varies with the pore-saturating fluids.

Fig. 4. The vug porosity-distribution profile-calibration results in the Well A (a) and Well B (b). Left to right, the first track is the depth in meter; the second track is the depth in feet; the third is GR, CAL log curves; the fourth is a dynamic-processing microresistivity image from FMI logging; the fifth is the vug porosity profile-processing result from image log; the sixth is LLS (R_S) and LLD (R_D); and the seventh is CGR log curve.

4.2.4. Total porosity partition: vug fraction quantification

The comparison between the density porosity and sum total porosity (PHISUM) demonstrates that there is a significant similarity between the two porosity depth-profiles at least in terms of data fluctuations despite the lack of exact spike-spike matches between them. The similarity became much better by applying a median filter to the two porosity curves (Fig. 5a and b, Track 12). The PHISUM represents the sum of the matrix or interparticle porosity, fracture porosity, and image log-derived vuggy porosity that are obtained separately (Eq. (1)). It suggests that the density tool would have responded to some secondary pore types, in addition to the interparticle pore space and fractures, and it may indicate the DEN log to be a suitable-total porosity estimator. These secondary pore types might likely be separate vugs, such as molds, shelter, and intraparticle space, which are commonly fabric-selective in origin similar to the interparticle porosity that can result from the selective secondary dissolution of cement or matrix (Choquette and Pray, 1970; Lucia, 1983; Lønøy, 2006; Bahrami et al., 2017). Additionally, it should also be noted that we have shown the density log responses are sensitive to the presence of fractures in the Fracture Porosity Characterization section. Therefore, the separate-vug porosity (φ_{sv}) can be determined by subtracting the sonic and fracture porosity from the density porosity (Eq. (2)). This assertion is applied to derive the separate-vug porosity by jointly inverting the conventional porosity and resistivity logs, and it has provided the starting point to decompose the total porosity into fractions of the identified pore types.

In the event that φ_{sv} obtained from the inversion of standard well logs (Eq. (2)) is larger than φ_{vim}, the difference (>0) may be associated with the presence of microporosity and/or intraparticle porosity, especially the micro-moldic separate-vug porosity ($\varphi_{sv\mu}$), Eq. (3). The microporosity estimate is relatively important at the depth intervals with relatively higher separate-vug and/or interparticle porosity, both obtained from wireline logs. This adjustment enables us to show that φ_{sv} cannot be larger than the total vug porosity (φ_v) and also the particles themselves may possess micropores, such as moldic micropores

(<10–$20\ \mu m$ pore diameter; Lønøy, 2006), which could not be resolved from borehole electrical image (0.2 μm resolution), taken into consideration that the imaging device can only enable the detection of pores larger than 5 mm diameter (Akbar et al., 1995; Meng et al., 2018). Based on the point made above, φ_v can be estimated by adding $\varphi_{sv\mu}$ to φ_{vim} (Eq. (4)); otherwise, φ_v can be represented by φ_{vim}, and thus $\varphi_{sv\mu}$ can be assumed equal to zero. We understand that this assumption may not necessarily be true, but it is believed to make a good point for the procedure. Thereafter, the proportion of connected vugs (φ_{cv}) can be defined as φ_v minus φ_{sv} (Eq. (5)). Finally, the total porosity can be estimated using Eq. (6).

$$\varphi_{sum} = \varphi_m + \varphi_f + \varphi_{v_{im}}, \tag{1}$$

$$\varphi_{sv} = \varphi_D - \varphi_m - \varphi_f, \tag{2}$$

$$\varphi_{sv\mu} = \varphi_{sv} - \varphi_{v_{im}}, \tag{3}$$

$$\varphi_v = \varphi_{v_{im}} + \varphi_{sv\mu}, \tag{4}$$

$$\varphi_{cv} = \varphi_v - \varphi_{sv}, \tag{5}$$

$$\varphi = \varphi_m + \varphi_{cv} + \varphi_{sv} + \varphi_f, \tag{6}$$

where φ_{sum} is the sum total porosity, and φ represents the total or bulk (PHIB) porosity; the others are as defined in the text and Appendix A.

In the presented scheme, when $\varphi_{vim} \leq \varphi_{sv}$, we can infer that $\varphi_{cv} = 0$ ($\varphi_{sv} = \varphi_v$), $\varphi_{sv\mu} \leq \varphi_{sv}$, and $\varphi = \varphi_D$ ($\varphi_{sum} = \varphi$); the rock texture may be a classical moldic mudstone, particularly if the matrix porosity is significantly very low. Conversely, when $\varphi_{vim} \gg \varphi_{sv}$, it can indicate that $\varphi_{cv} \neq 0$, $\varphi_{vim} = \varphi_v$ ($\varphi_{sv\mu} \approx 0$), and $\varphi > \varphi_{sum}$; for $\varphi_{cv} \gg \varphi_{sv}$, we can obtain a classical grainstone with very negligible microporosity ($\varphi_{sv\mu} \approx 0$), but $\varphi_f \neq 0$. Fig. 5a and b shows the depth-profiles of the different porosities in Well A and B, respectively.
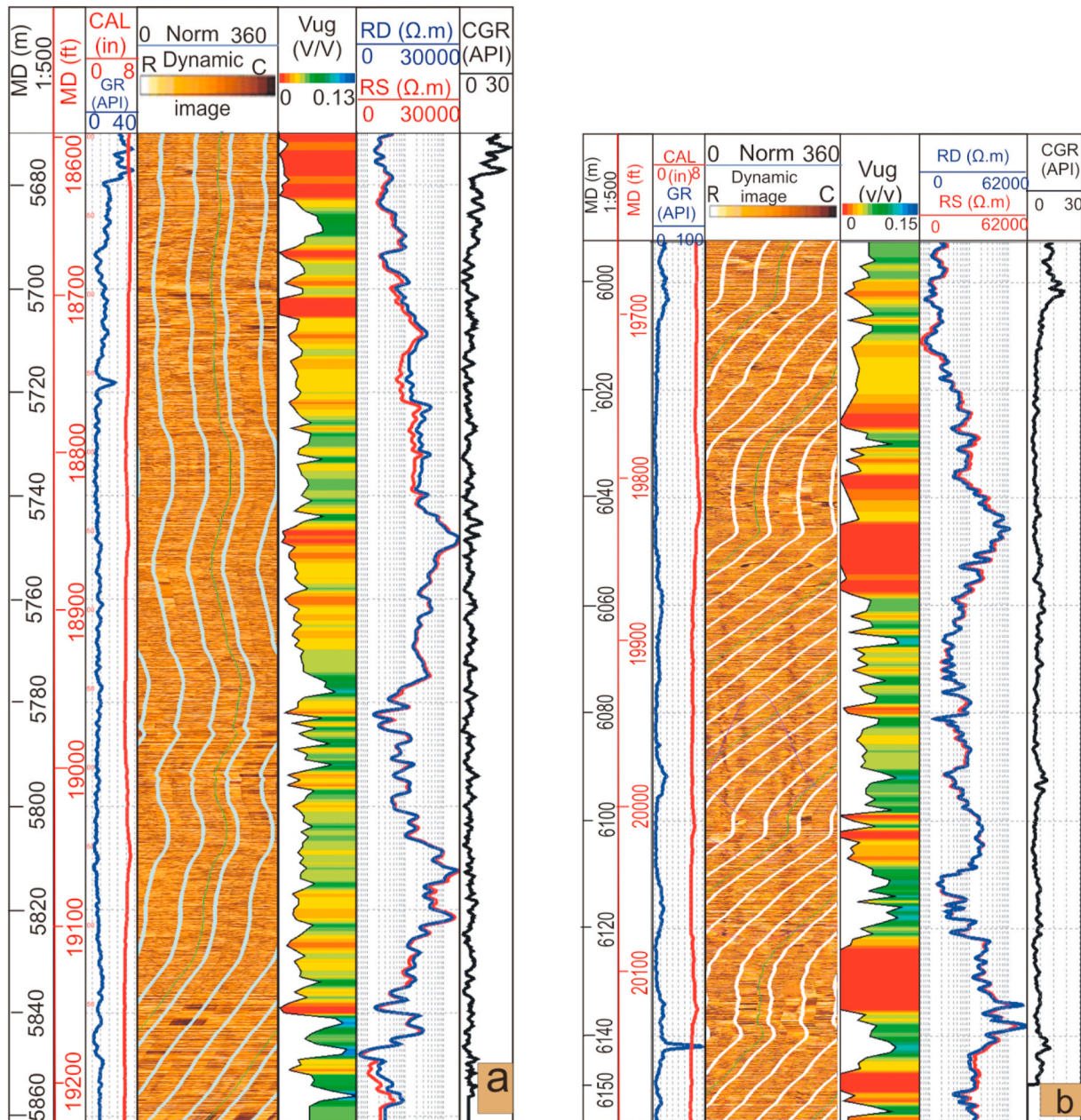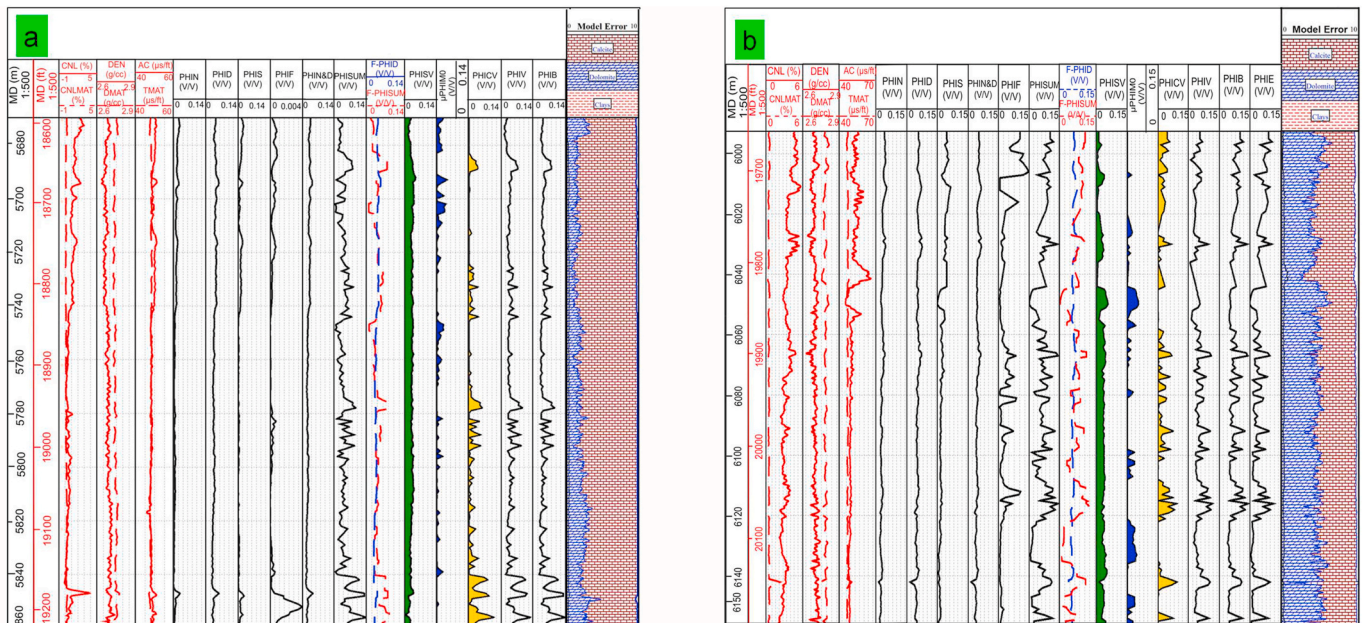

Fig. 5. The porosity partition-vertical distribution results in the Well A (a) and Well B (b). Left to right, the first track is the depth in meter (m); the second track is the depth in feet (ft); the third is the bulk and matrix CNL log curves; the fourth is the bulk and matrix DEN log curves; the fifth is the bulk and matrix AC log curves; the track sixth through eighteenth track is the CNL, DEN, AC, CNL-DEN, fracture, sum total, filtered density and filtered sum total, separate-vug, micro-moldic separate-vug, connected vug, total vug, bulk, and effective porosity. The track nineteenth is the elemental composition log as computed from multi-mineral analysis. Note the difference in fracture porosity horizontal scaling regarding its lower significance. The log effective porosity was not computed for Well A. Track 12 compares the density porosity and sum total porosity (PHISUM) after median filtering; the porosity-depth profiles show a significant similarity between them, indicating the density log can likely provide the total porosity estimate at least at intervals with a low abundance of secondary porosity, either touching or micro-moldic separate vugs.
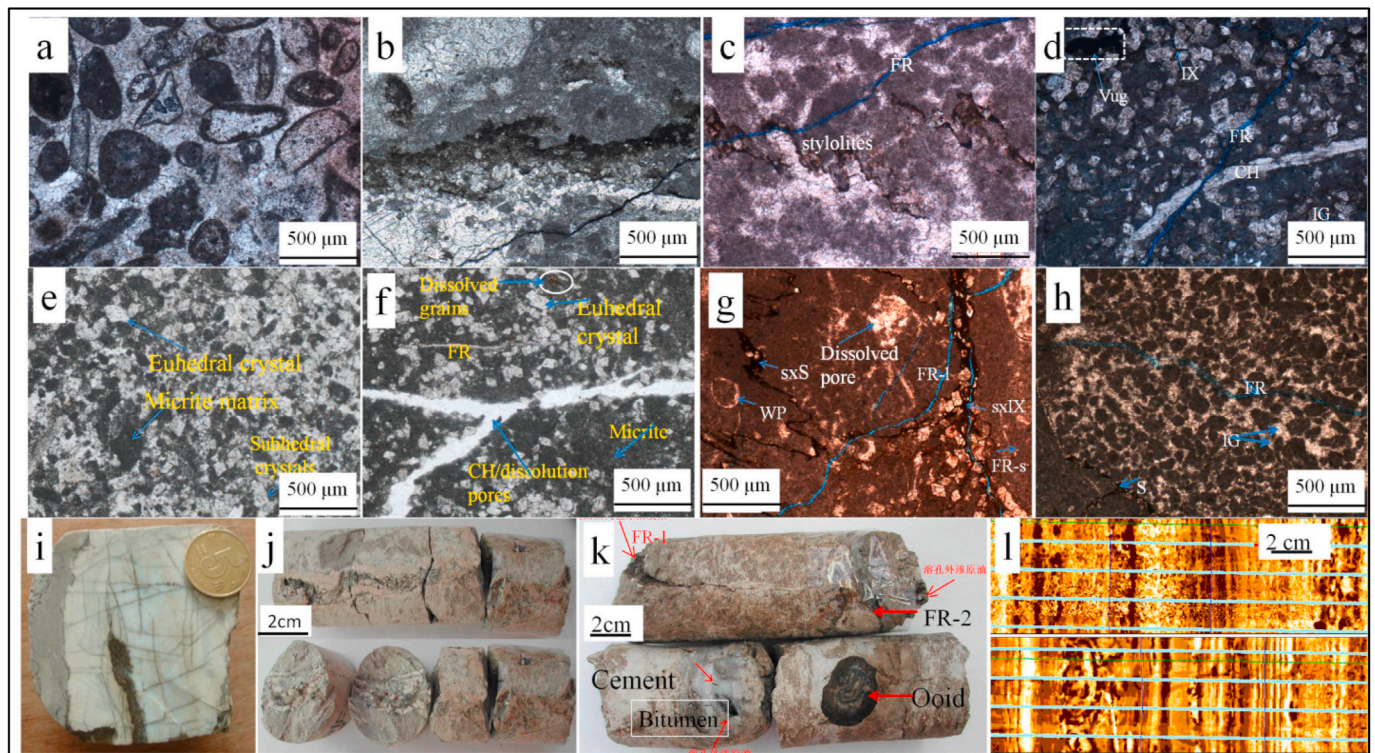
Fig. 6. The formation microfacies and pore type diversity in the studied Wells. (a) Skeletal grainstone. Note the occurrence of moldic pores and intragrain microporosity (Well A, 5691.45 m, O_2yj). (b) Fractured wackestone. Note pervasive leaching/corrosion through the rock fabric in the center, and large abundance of microcracks in lower and top right (Well A, 5693 m, O_2yj). (c) Fractured packstone. Note the enlargement of stylolites along the particle edges and cemented rich-primary porosity region in the center (Well C, 6148.6 m, O_1y). (d) Dolomitic packstone, interparticle pores (IG, IX). Note a channel (CH) cut by open fracture (FR), bitumen occupied the vug and IX, and high secondary porosity (Well C, 6149.89 m, O_1y). (e) Dolostones (Well D, 5961.27 m, $O_{1-2}y$). (f) Gray dolomitic mudstones (Well D, 5961.4 m, O1–2 y). Note a large channel (CH) or dissolution pore in the center. (g) Packstone fabric, intraparticle (WP) and dissolution pores, fractures (FR), solution-enlarged stylolites (sxS), and solution-enlarged intercrystalline pores (sxIX) filled with bitumen. Note the presence of fractures with small (FR-s) and large (FR-l) opening and cut by stylolites and solution. The porosity has been significantly improved (Well E, 6127.26, O1–2 y). (h) Fractured grainstone. Note abundant intergrain pores (IG) and corroded stylolites (ST) in the lower-right angle (Well E, 6127.44, O1–2 y). (i) Fractured rock fabric with isolated and large size vugs. Note two stage cross-cutting horizontal and vertical fractures with partial cementation of the first stage fractures (Well B, 6060.91 m, O_2yj). (j) Packstone, large scale solution-enlarged fracture filled partially by calcite and clastic materials (Well B, 5998.18 m, 5998.84 m, O_2yj). (k) Fractured-vuggy grainstone, isolated vugs (SV). Note the pore space is occluded by both calcite cement and bitumen, the low-angle FR-2 cut the cemented high-angle FR-1, and the large deformed ooid is dissolved and cemented (Well B, 6117.27 m, $O_{1-2}y$). (l) Bioclastic grainstone showing layering vugs and dark spot dissolution pores. Note a large ooid is deformed and dissolved (Well A, 5842–5844 and 5848–5850, $O_{1-2}y$). The data shows the significance of secondary processes on the evolution of depositional facies and reference porosity. The thin sections were impregnated with blue dyed resin, and the micrographs were taken under plane-polarized. Note: top core and FMI image is to the left. (For interpretation of the references to color in this figure legend, the reader is referred to the Web version of this article.)

4.3. Samples characteristics, core analysis and optical porosity estimation

The study formations are the Middle-Lower Ordovician Yingshan ($O_{1-2}y$) and Yijianfang (O_2yj) formations that contain the most prolific reservoir beds in Tahe Oilfield, North Tarim Basin. These strata are buried to over 5500 m, and approximate several hundreds of meters thickness in the studied Wells. They represent a shallowing upward and basinal prograding sequence deposited on a ramp-to-weakly rimmed marine platform under relatively shallow water (~20 m depth) and high-energy current settings. The logged interval can be subdivided into two, three, and six sequences of 2nd, 3rd, and 4th order, respectively. The 2nd order lower and upper sequence defines a transgressive and high-stand system tract, respectively, and a third- and fourth-order sequence comprises a retrogradational cycle underlying a progradational cycle. The sedimentation and stratigraphic architecture have mainly evolved with the changes in the relative sea-level in response to the variations of the regional/local climate phases and tectonics (Yu et al., 2001, 2016). Microfacies analysis based on thin-section petrography and core analysis and image log interpretation demonstrated that the Yingshan ($O_{1-2}y$) and Yijianfang (O_2yj) formations developed mainly in an open-restricted platform (intraplatform shoal and depression) and open platform (intraplatform shoal and patch reefs) environments,

respectively (Ning, 2017; Meng et al., 2018). Typical microfacies include (i) intershoal sea microfacies (ISMF) (ii) low-energy shoal microfacies (LSMF) (iii) high-energy shoal microfacies (HSMF) (iv) lagoon microfacies (LMF) and (v) tidal flat microfacies (TFMF) (Li et al., 2016; Meng et al., 2018). The Yingshan ($O_{1-2}y$) stratum comprises largely dolostones and argillaceous limestone (dolomitic mudstone, mudstone, packstone, and grainstone rock fabrics), whereas the Yijianfang (O_2yj) Formation consists essentially of limestones (mudstone-wackestone, bioclast packstone, and intraclast packstone rock fabrics) such as algal limestone, clastic limestone, and bioclastic limestone. The reservoir rock matrix consists volumetrically of limestone and dolomitic limestone lithology with a very low and variable content of clay-type particles.

The drill cores and thin-sections as shown in Figs. 1 and 6 clearly demonstrate the evidence of complex diagenetic history involving the reworking of original facies and associated pore systems. Secondary mechanical and chemical compaction-related pressure solution, dissolution-karstification, cementation, and recrystallization were the major post-depositional processes that have influenced the evolution of the depositional facies, and the pore structure types. The samples can show that stylolites and micro-fractures are commonly present in the study formations. The cementation led to partial occlusion of the

primary pore space, and the dolomitization of original formation texture was critical in the evolution of porosity, i.e. intercrystalline porosity creation. The dolomite crystals are subhedral to euhedral, and they vary in size from fine to coarse crystals. The critical mechanisms for reservoir development include dissolution (leaching), karstification, and hydrothermal alterations (Jin et al., 2009; Zhu et al., 2015; Guo et al., 2016; Liu et al., 2017). Regions of higher original porosity might have provided routes for fluid circulation and dissolution, particularly in grainstones and packstones with relatively high permeability (Smith et al., 2003; Lønøy, 2006; Liu et al., 2017; Ning, 2017).

4.3.1. Core analysis porosity

The core samples were selected and analyzed at the Experimental Research Center of Wuxi Research Institute of Petroleum Geology of SINOPEC using the GB/T29172-2012 method. The full-diameter core porosities were measured using the gas porosimeter YK-98, YQ2-98-01. The values obtained ranged from 0.1% to 3.4%, with an average value of 1.25%. Considering the only six cored Wells, and the accuracy of core laboratory measurements is a critical factor for successful data evaluation, Wells A and B show more reliable analysis data that were applied to calibrate the log-derived porosities. We used the optical porosity (PHIO) derived from digital thin-section image analysis for Well A, and full-diameter core porosity measurements for Well B, respectively.

4.3.2. Thin-section image analysis: 2D optical porosity determination

Despite the lower limit of the sampling scale of 1 in. diameter size, thin-section imaging provides images with very high resolution that can allow rock-pore typing in carbonates, in a sense that, it is possible to distinguish the rock grains, matrix, and types of cement, and matrix porosity, fractures, and vugs. Additionally, the technique is practically cheap, quick, and simple to be applied (Tonietto et al., 2014; Voorn et al., 2015; Buono et al., 2019). However, thin-section imaging is a destructive technique.

The micrographs were acquired using the procedure given in Appendix B. To quantify the porosity, the segmentation of thin-section was found to be problematic using *Adobe Photoshop* because of the possibility of segmenting the rock matrix as pores, and this can lead to overestimating the amount of the pixels representing the porous space. This

situation is common in image segmentation routines with some techniques working better than others (Wardaya et al., 2013; Voorn et al., 2015). To address this segmentation issue, the *Image-Pro Plus* software, which has a suite of necessary processing tools and well-structured steps thereby enabling to achieve successful image segmentation, was used to perform the image pre-processing and segmentation. We first set the system spatial calibration, in this case, set at 5X, before the image pre-processing which involved image contrast enhancement and image spatial and intensity calibration. We applied single spatial and intensity calibration, set at 5x and Cal 49, respectively, to all the thin-section images. The images were segmented using both the Histogram and Color Cube-based methods depending on the pore structure heterogeneity, i.e. the presence of multiple pore types (Fig. 7). For convenience, the segmented images were then imported into *Adobe Photoshop* for automatic pixel counting, though it could also be carried out through the "Count/Size" command without exporting the images. Finally, for a single micrograph, the optical porosity (PHIO) is determined as the ratio of pore-related pixel counts (X_{Mi}) to the total amount of pixel in that micrograph (Y_{Mi}), Eq. (7a). For a given thin-section, PHIO is defined as a weighted average of X_{Mi} of the different captured micrographs, where Y_{Mi} of the different micrographs are the weights, Eq. (7b). Additionally, the weighted average value is determined for a sample with multiple thin-sections to ensure data representativeness. When Y_{Mi} is identical for all the micrographs captured from a given thin-section, the weighted average is simply equivalent to the arithmetic one, Eq. (7c). We suggest applying Eq. (7b) to account for the variations of pixel content in case of different object-related geometries, such as irregular shapes, capturing micrograph near the thin-section edges, and sampling a section of interest (SOI).

$$P = \frac{X_{Mi}}{Y_{Mi}} , \tag{7a}$$

$$P' = \left(\sum_{i=1}^{N} P Y_{Mi} \right) \bigg/ \sum_{i=1}^{N} Y_{Mi} , \tag{7b}$$

$$P' = \frac{1}{N Y_M} \sum_{i=1}^{N} X_{Mi} , \tag{7c}$$
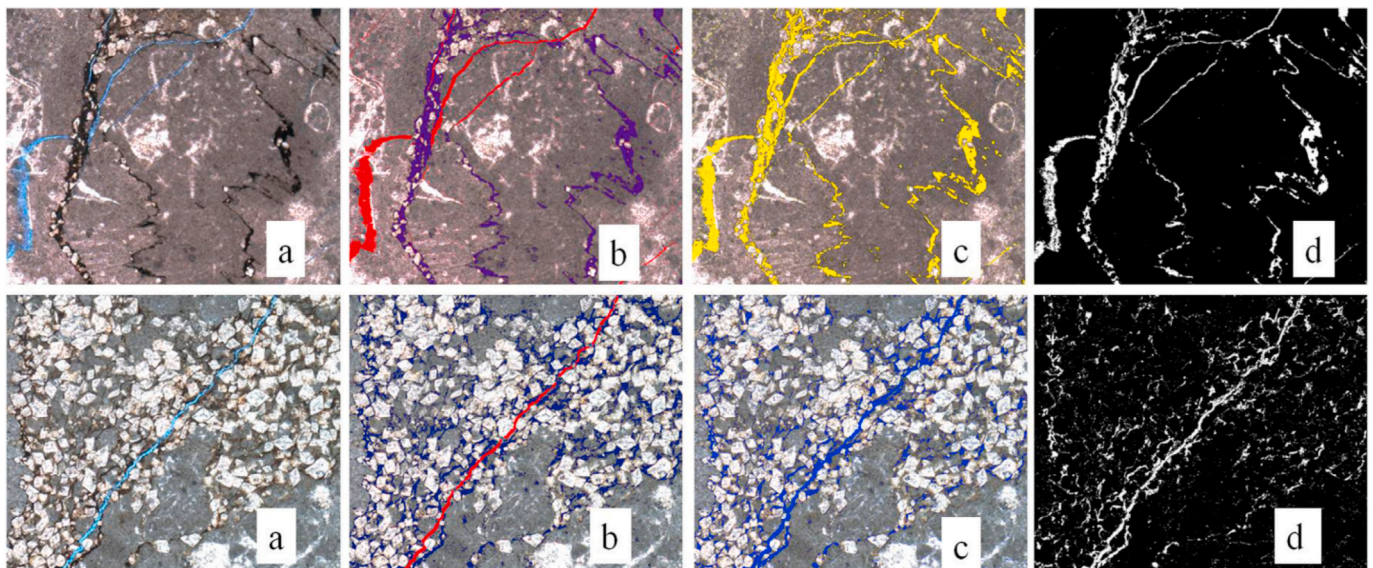
Fig. 7. The thin section segmentation procedure-illustration-pore feature extraction results based on two thin-section photomicrograph samples. (a) Initial 24-RGB image. (b) Segmented image using Color cube-based technique using two color classes, red and dark-blue color classes indicate epoxy-filled fractures and dark objects (stylolites and interparticle pores), respectively. The dark features show generally lower intensity than the rock grains. (c) Image in (b) segmented using one color class. (d) Binary image. Porosity is displayed as white, and the grains are black. (For interpretation of the references to color in this figure legend, the reader is referred to the Web version of this article.)

where the P and P' are the PHIO and weighted average PHIO related to a micrograph and a thin-section, respectively, X_{Mi} is the pore-related pixel count in a micrograph, Y_{Mi} is the micrograph pixel amount, N is the number of micrographs for a given thin-section, and i refers to the ith micrograph for each thin-section.

4.4. Derivation of the vuggy porosity models

The foundation of the basic theory of secondary porosity estimation from logs arises from the observation that standard acoustic logging devices do not almost detect spherical void space, i.e. vuggy and moldic pore types (Lucia and Conti, 1987; Wang and Lucia, 1993; Dehghani et al., 1999). Accordingly, there have been developed many acoustical approaches for decomposing total porosity into relative fractions of individual basic pore types based on the deviation of the velocity or porosity calculated using the Wyllie equation from the measured velocity or the porosity obtained mostly from the CNL-FDC logs, and core samples, as the case may be. Additionally, borehole imaging methods have been applied to portion the total porosity into primary porosity, and secondary porosity composed of vugs and fractures. Table 1 shows a sample of existing models for calculating vuggy porosity.

To establish the vuggy porosity models, we developed a modified Lucia's approach (Lucia and Conti, 1987), which involves relating the vug fraction to the pseudomatrix interval transit time, Δt_{ma}, referred to as acoustic intercept. Characteristically, the acoustic intercept represents the acoustic slowness, expressed in microseconds per feet (μsec/ft), related to 0% porosity on a crossplot of porosity against interval transit time ($\varphi - \Delta t$). The acoustic intercept equation is defined as a multivariate transform involving the density and velocity of the bulk rock, matrix, and fluids, total porosity, and composition of the rock matrix, and fluids as the variables. To this end, we considered 3 intercept cases, and each case with 4 scenarios, which resulted in twelve models (Table 2). The models were designed as *MISA*, where the letters *I*, *S*, and *A* are the intercept or acoustic transform, scenario, and applied equation, respectively. The models were comparatively evaluated based on their prediction accuracy.

As can be seen in Table 2, the intercept case 1 and case 2 and 3 are modified forms of the Wyllie time-average equation, and the generalized Wyllie equation, respectively, with the porosity (φ) is substituted for the sonic and bulk porosity, respectively (Wyllie et al., 1956; Saleh and Castagna, 2004). Additionally, it can be seen that the M122 may represent a typical Lucia's model (Lucia and Conti, 1987). The parameter s in the intercept equations (cases 2 and 3) is a pore shape factor that can be determined using the bulk, matrix, and fluid velocities, and the bulk porosity (Saleh and Castagna, 2004).

Based on the porosity partition scheme presented above, Eq. (1) through Eq. (6), we have defined two transforms, C and C′, which were then related to the total-vug and separate-vug porosities to derive the total-vug and separate-vug porosity models, respectively. The transforms C and C′ are the established acoustic intercept equations with the porosity (φ) is substituted for the total porosity and density porosity, respectively. Additionally, two pore shape factors, s and s′, are defined using Eqs. (8a and 8b) and involved in the C and C′ transforms,

Table 1
Sample of equations used for estimation of vug porosity from log responses.

CASE	INTERCEPT (I)	SCENARIO (S)	APPLIED EQUATION (A)
1	$\Delta t_l - (\Delta t_f - \Delta t_{ma})\varphi$	(1) φ_V vs. I	(1) $\varphi_V = A + B.I$
2	$\left[\Delta t_l - (\Delta t_f - \Delta t_{ma}^s)\varphi\right]^{\frac{1}{s}}$	(2) $\log(\varphi_V)$ vs. I	(2) $\varphi_V = 10^{A + B.I}$
		(3) φ_V vs. logI	(3) $\varphi_V = A + B.logI$
3	$\left[(\Delta t_l - \varphi\Delta t_f)/(1-\varphi)\right]^{\frac{1}{s}}$	(4) $\log(\varphi_V)$ vs. logI	(4) $\varphi_V = 10^{A + B.logI}$

Note: the numbering for the scenarios and applied equations are matched consistently.

Table 2
The modeling elements and structure.

		11				22				33				44 a			
		RMSE	R^2	MD	MR	RMSE	R^2	MD	MR	RMSE	R^2	MD	MR	RMSE	R^2	MD	MR
Case 1	PHIV	0.270	0.980	0.070	1.018	0.939	0.876	−0.036	1.004	0.298	0.974	0.004	0.996	1.164	0.844	−0.023	1.010
	PHISV	0.269	0.821	−0.057	0.978	0.363	0.699	−0.001	1.006	0.267	0.816	−0.005	0.995	0.368	0.689	0.013	1.010
Case 2	PHIV	0.346	0.966	−0.066	0.996	0.299	0.966	−0.006	1.004	0.190	0.989	−0.002	1.003	0.586	0.931	−0.021	1.005
	PHISV	0.138	0.952	−0.026	0.991	0.234	0.846	0.010	1.009	0.143	0.947	0.005	1.000	0.255	0.818	−0.001	1.006
Case 3	PHIV	0.284	0.984	0.161	1.062	0.498	0.950	−0.018	1.004	0.178	0.991	0.003	0.997	1.077	0.879	−0.030	1.008
	PHISV	0.184	0.958	−0.132	0.954	0.233	0.845	0.004	1.007	0.136	0.952	−0.003	0.997	1.256	0.815	−0.001	1.006

Table 3
Computed statistical parameters for evaluation of the modeling results: a. Well A; b. Well B.

		11				22				33				44 b			
		RMSE	R²	MD	MR	RMSE	R²	MD	MR	RMSE	R²	MD	MR	RMSE	R²	MD	MR
Case 1	PHIV	0.308	0.985	0.141	1.041	0.784	0.877	−0.040	1.008	0.279	0.984	0.000	0.996	0.916	0.849	−0.026	1.013
	PHISV	0.260	0.946	−0.002	0.988	1.426	0.781	−0.077	1.054	0.275	0.94	0.006	0.988	1.599	0.758	−0.091	1.055
Case 2	PHIV	0.444	0.962	0.098	1.418	0.353	0.953	−0.044	1.001	0.236	0.989	0.003	1.018	0.582	0.909	−0.034	1.008
	PHISV	0.156	0.983	0.050	1.023	0.940	0.859	−0.083	1.026	0.155	0.981	−0.005	0.990	1.258	0.810	−0.089	1.045
Case 3	PHIV	0.319	0.982	0.103	1.035	0.504	0.932	−0.025	1.008	0.171	0.994	0.002	0.996	0.879	0.859	−0.039	1.010
	PHISV	0.147	0.984	−0.043	1.015	0.942	0.857	−0.084	1.034	0.155	0.981	0.002	0.991	1.282	0.803	−0.089	1.046

Note: PHISV = separate-vug porosity model; PHIV = total vug porosity model; PHIO = thin-section optical porosity; RMSE = root mean square error in porosity; R² = coefficient of determination; MD = mean departure (in porosity unit); and MR = mean ratio of the actual measured to fitted value (dimensionless). Columns are designed such as: the first number indicates scenario, and the second number is related to the applied equation.

respectively, for the intercept cases 2 and 3. These equations represent the Saleh and Castagna' equation (Eq. (8) in their paper) with the total porosity (φ) and density porosity (φ_D) is substituted for the bulk porosity (φ_B), respectively.

$$s = \frac{Log\left[(1-\varphi)V_{P_l}V_{P_f}\right] - Log\left(V_{P_f} - V_{P_l}\right)}{Log V_{P_{ma}}} \quad, \tag{8a}$$

$$s' = \frac{Log\left[(1-\varphi_D)V_{P_l}V_{P_f}\right] - Log\left(V_{P_f} - V_{P_l}\right)}{Log V_{P_{ma}}} \quad, \tag{8b}$$

where s and s' are the pore shape factors (dimensionless) used in the C and C' equations, respectively, φ and φ_D represent the total and density porosity, respectively (fraction). V_P is the compressional acoustic velocity of the bulk rock, the matrix and the fluid (in km/sec).

Fig. 8a and b show the results of the total-vug and separate-vug porosity modeling, respectively, for Well A, and Fig. 8c and d show the results of the total-vug and separate-vug porosity modeling, respectively, for Well B. For each model, the prediction trendline varies with the model type, i.e. the case and scenario, and provides an initial qualitative mean to verify the modeling stability and reliability. It is interesting to observe that the trendlines exhibit almost a similar pattern for a given scenario for both the total-vug and separate-vug porosity models, though there are subtle differences according to the applied intercept equation in the two Wells A and B. Importantly, the trendline describes a straight line that follows almost a 1:1 trend for the scenarios 1 and 3 for the three intercepts, which show that the vug porosities relate well to the acoustic intercepts in all the three cases. Contrarily, there is a great deviation and scatter around the trendlines in the case of scenarios 2 and 4 for the three intercepts. Thus, the acoustic intercept–vuggy porosity relationships cannot presumably enable accurate vuggy porosity prediction.

4.5. Verification of the porosity estimation

Because the vug fractions (total and separate vugs) are key inputs involved in the vuggy porosity modeling, we evaluated the accuracy of the newly-developed procedure for total porosity determination and partition into its components. We compared the log-derived total and effective porosity to the thin-section optical porosity (PHIO) and core porosity, respectively. Fig. 9a compares the bulk porosity obtained from logs to PHIO derived from thin-section image analysis for Well A. The results show a significant match with less scattering of data as revealed by the coefficient of determination ($R^2 = 0.86$), indicating a good correlation. The calculated magnitude error of 1.37 in the porosity unit is generally acceptable, and it falls within the common value range for carbonate reservoirs. The calibrated porosity data define a highly comparable variation profile, which overlaps the log porosity-depth profile but slightly shifts away in the upper logged interval. Overall, the comparison is generally of high quality. Therefore, this can support the application of the resulting regression equation for predicting the total porosity in uncored wells locally with the log-derived total porosity available. Fig. 9b compares the effective porosity obtained from logs with the full-diameter core porosity for Well B. The log-derived effective porosity is calculated as the difference between the total and separate vug porosity, both obtained from the wireline logs. The crossplot shows that the two porosity data are poorly related, $R^2 = 0.17$. The poor correlation may partly relate to other considerations, rather than the entire methodology itself.

The uncertainty related to accurately defining the core-plug depth location may contribute to the mismatch between the log and core porosity (Tyagi and Bhaduri, 2002). In addition to the common core-plug sampling challenges in carbonates (e.g. low sample-to-vug size ratio, and systematic core plug retrieval from intact core sample), the accuracy of core porosity measurement can be affected by laboratory experimental issues, such as incomplete sample saturation, and fluid
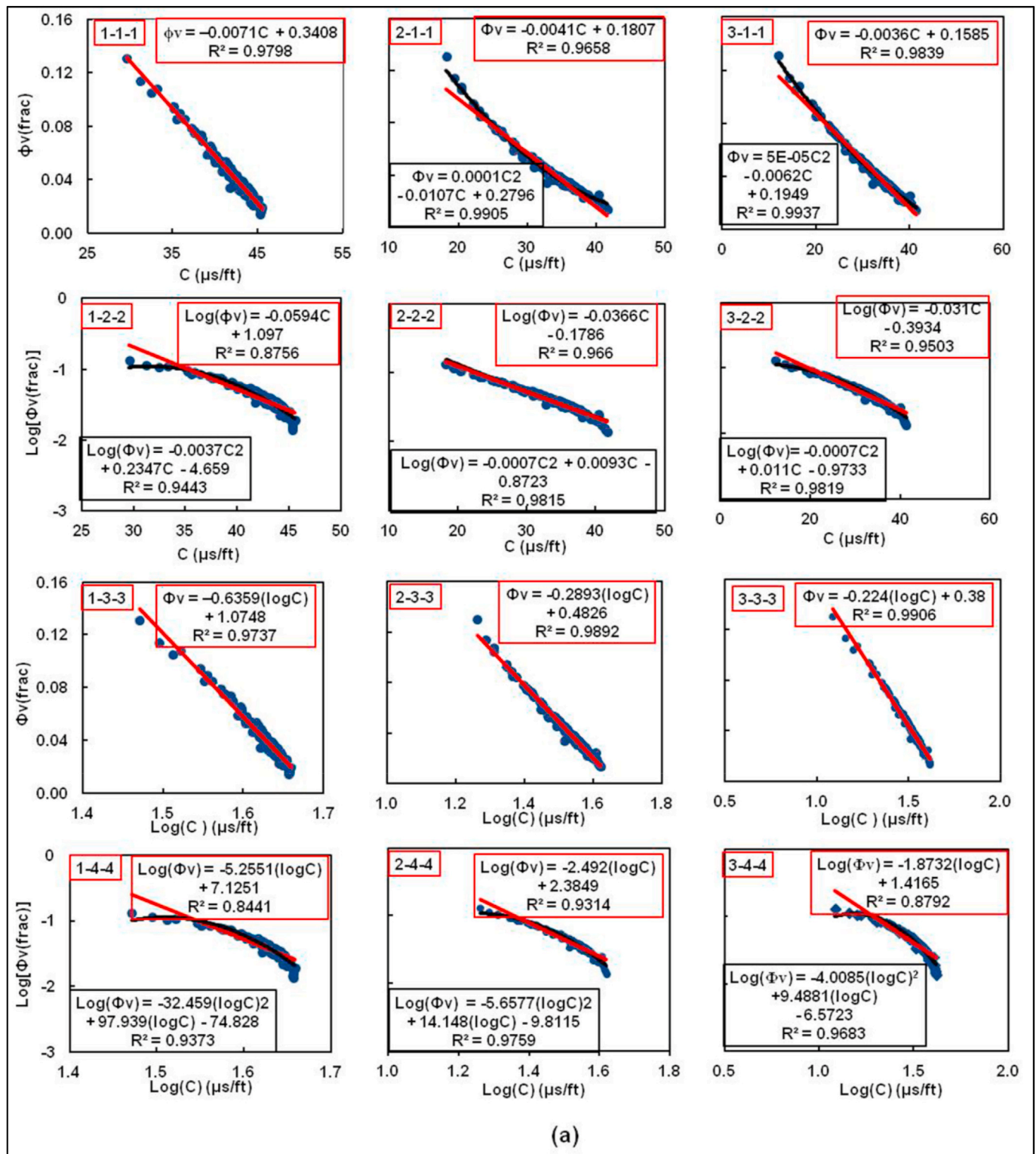
Fig. 8. The acoustic velocity–vuggy porosity relationship-total and separate vug porosity modeling results in the two Wells A and B. (a) and (b) show the total-vug and separate-vug porosity models, respectively, for Well A. (c) and (d) show the total-vug and separate-vug porosity models, respectively, for Well B. On each diagram, the red box in the top upper-left is the model code or identifier, and the red trendline and red text box in the top upper-right show the trendline relation and coefficient of determination, respectively, are related to the linear fit. Also, on some diagrams, the black trendline and text box in the bottom shows the trendline relation and coefficient of determination are related to the second-order polynomial fit. (For interpretation of the references to color in this figure legend, the reader is referred to the Web version of this article.)
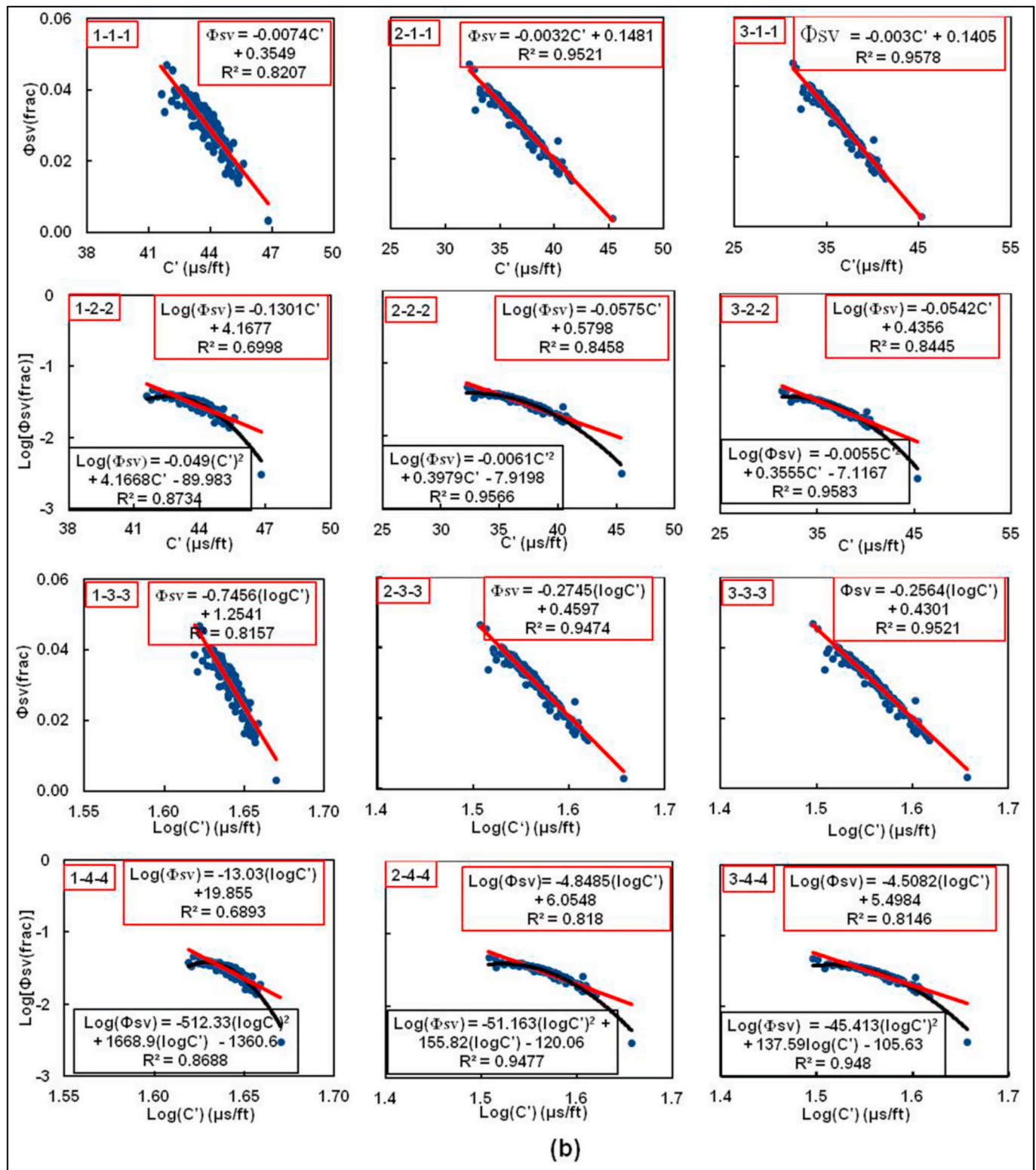
Fig. 8. (*continued*).

adsorption. Additionally, because porosity is a scale-dependent rock property, the heterogeneity that increases from megascopic to microscopic scale could heavily contribute to the discrepancies between core and log-derived porosities (Vik et al., 2013; Sadeghnejad and Gostick, 2020). Core porosity generally represents the interconnected (effective) porosity, which cannot easily be obtained using the standard porosity logging methods. Besides the separate-vug porosity that is considered to

negligibly contribute to flow, the matrix porosity may be composed of inter- and intra-particle porosity and microporosity that can be poorly interconnected to the fractures and connected vugs (Lønøy, 2006). Taking into consideration the point stated above, for comparable depth, we corrected the core porosity by adding the core measured porosity to the log-derived connected-vug porosity, which usually dominates largely the interconnected pore networks (Lucia and Conti, 1987;
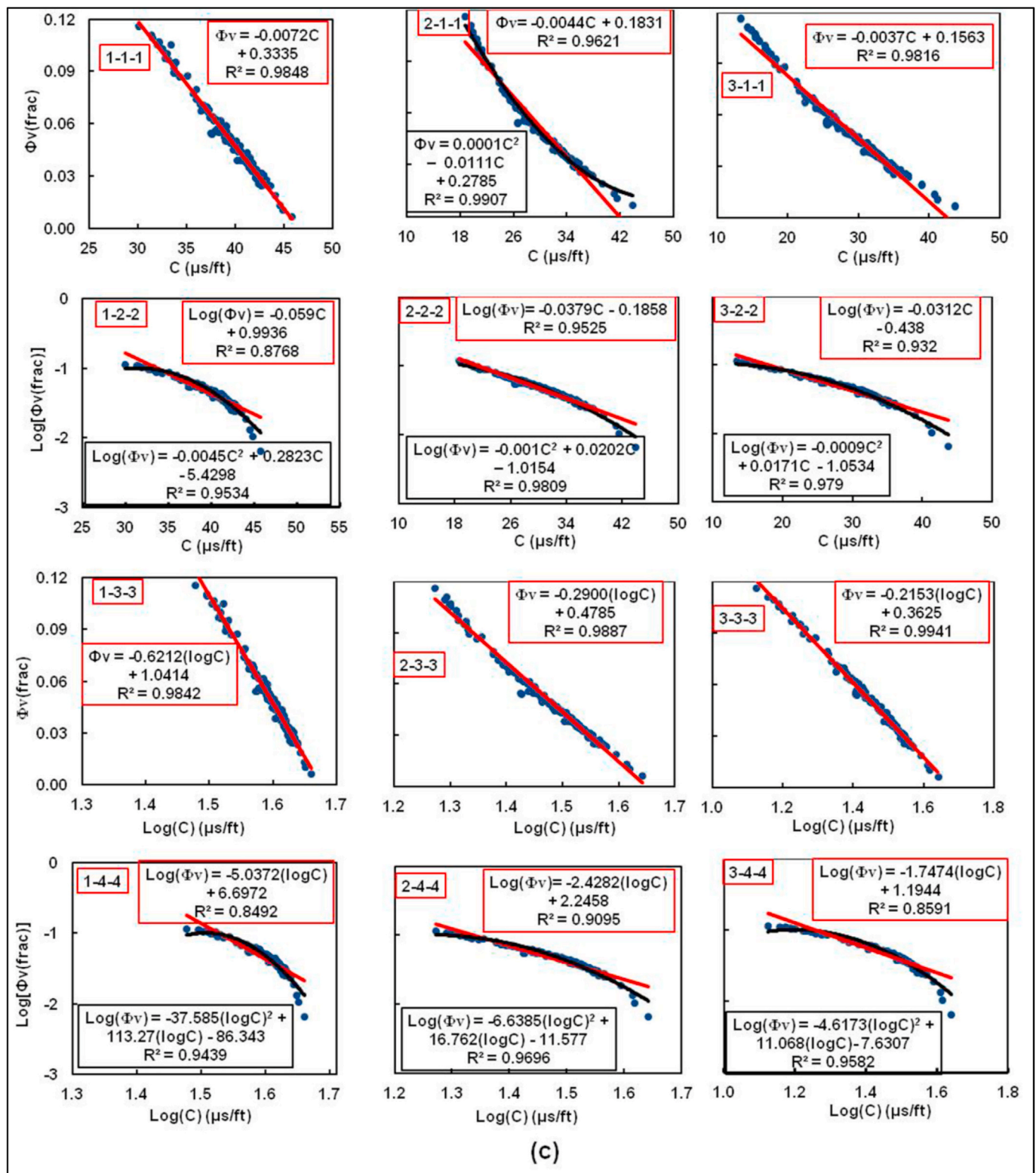
Fig. 8. (*continued*).

). After the correction, the porosity increased and each point shifted closer to its pair that was inverted from logs, and the profile of the calibrated core porosity reproduces closely the variations of the log-derived effective porosity profile. The correction has resulted in a relatively improved correlation.

4.6. Evaluation of the models

We examined the prediction accuracy of the different models by taking some computed parameters, such as the coefficient of determination (R^2), the root mean square error (RMSE), the departure (D), and the ratio of actual measured to predicted value (R), as the measures. Treating the determined vug fractions as error-free, that is, as the actual
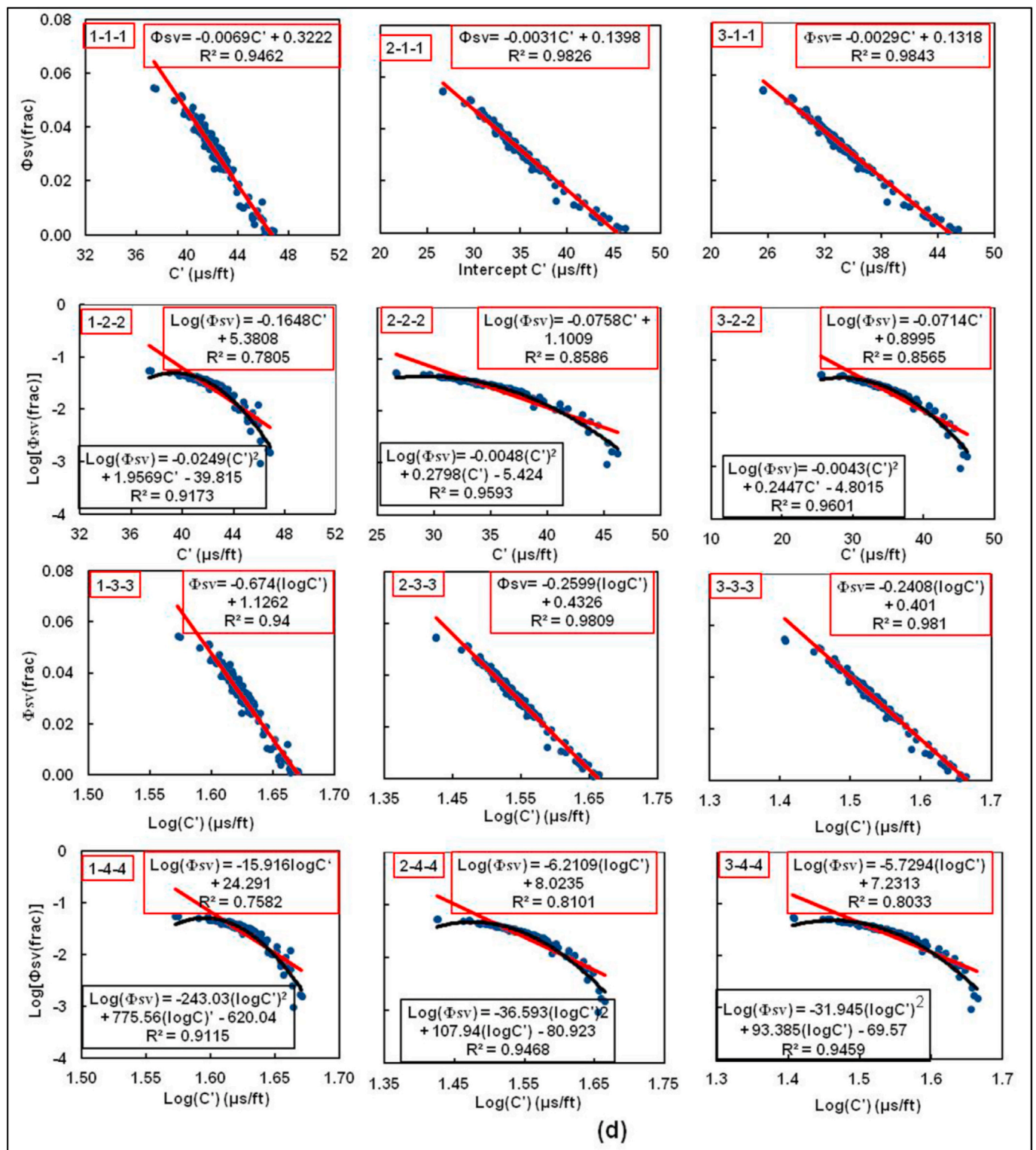
Fig. 8. (*continued*).

measured values, we can statistically evaluate the accuracy of the models. For simplicity in comparison, we computed the predicted values using only the linear trendline relation, though some models show a second-order polynomial best-fit with a relatively high R^2, particularly the case of scenarios 2 and 4 related models for the three intercept equations (Fig. 8a–d).

Fig. 10a and b show the variation of the departure and ratio parameters with the actual vug fractions (total and separate vugs) for the Wells A and B, respectively. The departure is defined by subtracting the vug fraction (total and separate) predicted based on a fitted-model from the actual measured one. The figures clearly show there are obvious differences between the different models. The higher deviation is observed in the distribution of the R parameter, which can define an essential parameter to evaluate the modeling accuracy, compared with the D parameter that exhibits less spread for the total-vug and separate-vug porosity modeling in the two Wells, A and B. However, it can be seen
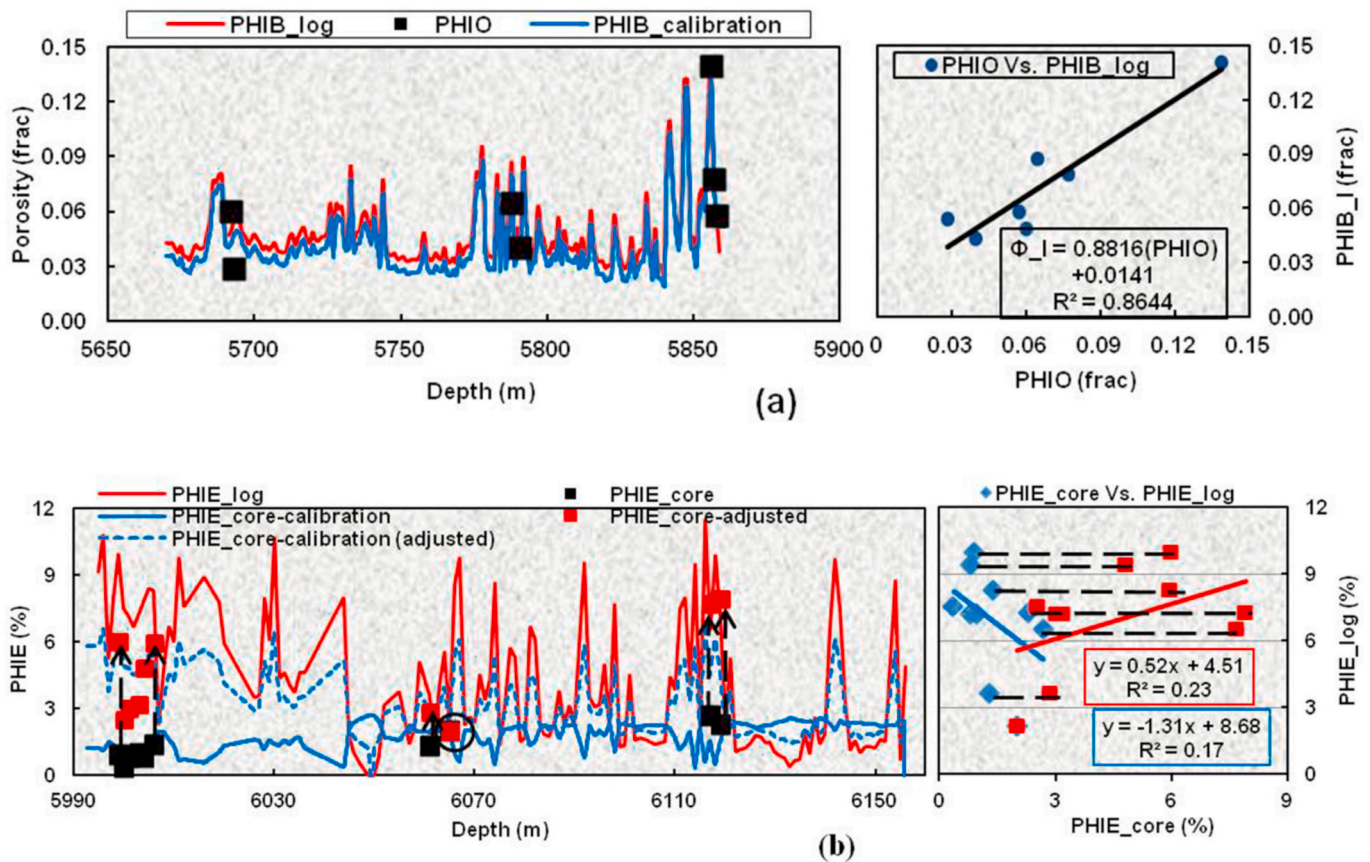
Fig. 9. The porosity-comparison-calibration, profile (left) and graphic (right) comparisons in the two Wells A and B. (a) Comparison between the log-derived bulk (total) porosity and 2D-optical porosity as determined from thin section image analysis for Well A. The coefficient of determination ($R^2 = 0.86$), RMSE (1.37 in porosity unit), and porosity profiles demonstrate a good match between the porosity values, indicating the validity of the interpretation results. The red and blue profiles represent the log and calibrated bulk porosity, respectively. The black square is the measured PHIO. (b) Comparison of effective porosity as calculated from logs and laboratory core porosity. A poor match is demonstrated by the low coefficient of determination ($R^2 = 0.17$) and the calculated RMSE of 5.44 in porosity unit. The good match observed at some specific depth-points, indicated by black circles, suggests there might have other factors contributing to the present discrepancy (see text). After the correction of core porosity, the values increased and the points (red square) shifted much closer to the log values for comparable depth, and the calibration porosity profile (blue dashed line) reproduces closely the trends of the log effective porosity. The blue and red boxes showing the trendline relation and coefficient of determination are related to the fitted measured and corrected porosity, respectively. (For interpretation of the references to color in this figure legend, the reader is referred to the Web version of this article.)

that the spread in the *D* and *R* parameters is less significant for the models M333 and M233, with the mean *D* and *R* values very close to 0 and 1.0, respectively. Thus, it can imply that these models can allow more satisfactory vuggy porosity prediction.

Table 3a and b show the computed statistical parameters used for further evaluation of the prediction accuracy of each model for Well A and Well B, respectively. For the linear models, again, based on the *RMSE* and R^2 parameters, the results speak for themselves, and they confirm that the model M333, to some extent M233, presents by far the ultimate accuracy, indicating that they can enable achieving considerably better prediction accuracy. Nevertheless, based on R^2, it can be seen that models M211 and M311 can provide satisfactory results, particularly for separate-vug modeling. However, these models sometimes require a second-order fit to obtain the best trendlines (Fig. 8a–d), and they carry relatively high *RMSE*. Additionally, they are characterized by a large spread in the distribution of the *D* and *R* parameters (Fig. 10a and b), which show mean values significantly different from 0 to 1.0, respectively. The predicted porosity values are both higher and lower than the actual measured ones for total and separate vuggy porosity. Therefore, it can be concluded that these models can lead to over- and under-estimating the vuggy porosity fractions. Moreover, the results show that the models M111 and M133 have a reduced prediction significance based on the *RMSE*, and the distribution of the *D* and *R*

parameters despite they are linear. But, it appears that the model M133 can provide a good approximation of vuggy porosity regarding the associated very low mean departure value approaching zero.

The results clearly demonstrate that the nonlinear models show less prediction accuracy, which gets improved from the intercept case 1 to cases 3 and 2, respectively. These models necessarily require a second-order polynomial fit to achieve a relatively good match for each intercept case (Fig. 8a–d), and they present the highest and lowest *RMSE* and R^2, respectively (Table 3a and b). Additionally, there is a large spread in the distribution of both the *D* and *R* parameters and their mean values deviate significantly from 0 to 1.0, respectively, though the models M244 and M344 show unexpected mean departure values very close to 0, particularly for separate-vug porosity models for Well A. The predicted vuggy porosities are systematically either larger or smaller than those directly interpreted, i.e. there is over- and under-estimation of the vuggy porosity. The lowest prediction accuracy is related to the scenario 4-based models, particularly the M144 model.

As shown in Fig. 8a–d and Table 3a and b, according to the graphical comparisons and statistical calculations, the values obtained and trend characteristics are similar for each model for the total-vug and separate-vug porosity models in the two Wells, A and B. This demonstrates the robustness and applicability of the porosity partition procedure and vuggy porosity modeling. The results suggest that the linear models, in
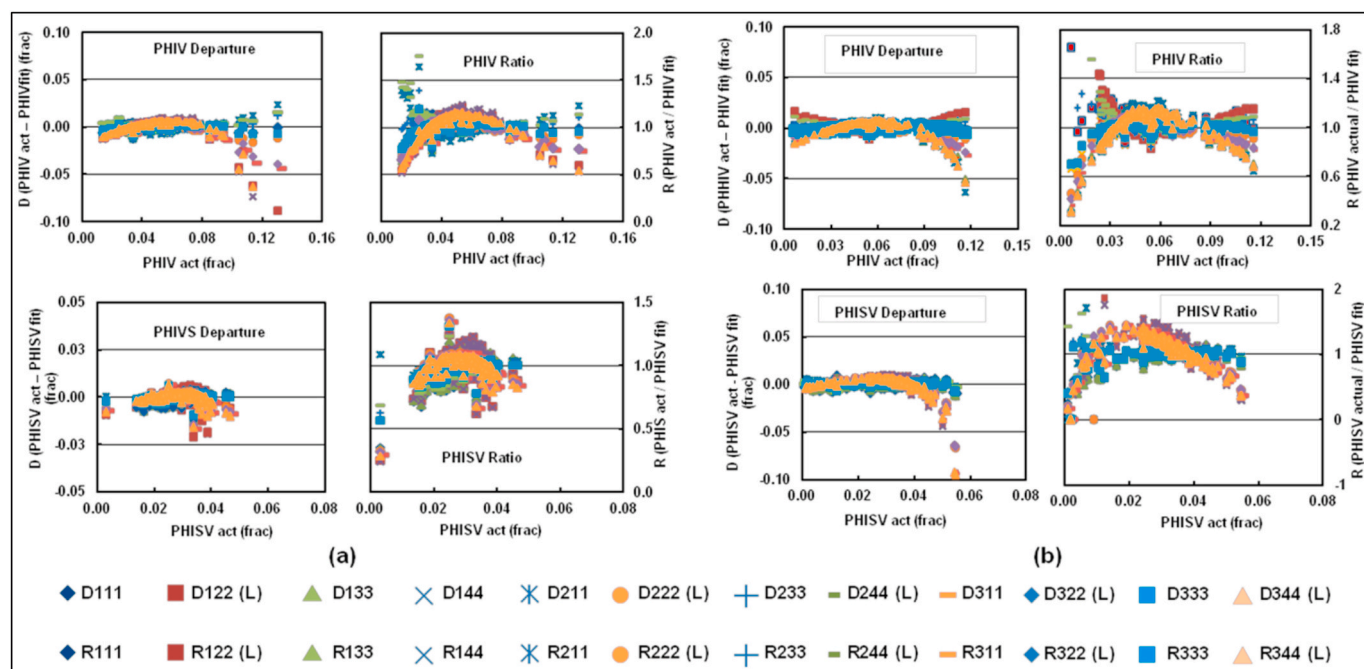
Fig. 10. The modeling stability determination-statistical parameters calculation-variation profile in the Well A (a) and Well B (b). On the left, diagrams of the departure (residual) vs. actual total-vug and separate-vug porosity at the top and bottom, respectively; on the right, diagrams of the ratio of actual measured to fitted values vs. actual measured total-vug and separate-vug porosity at the top and bottom, respectively. It can be observed that the models present different prediction abilities with the ratio parameter indicates significant spread in the predicted data variation, compared with the departure parameter. The higher stability "better match between measured and predicted value" is shown by the D &R333 and D&R233 profiles in the case of both total and separate vug modeling in the two Wells A and B.

particular, the models M233 and M333, relate much better the vug fraction to the acoustic intercept and enable better vuggy porosity estimation. In contrast, the nonlinear models display a greater deviation, that is, over- and under-estimation trends for relatively low (<4%) and high (>8%) vuggy porosity values, respectively, and they are characterized by lower R^2 even applying a second-order best-fit, especially the models M122 and M144. Also, the results show that the application of the nonlinear models is restricted over a less wide porosity range according to the trendline patterns.

The increased modeling accuracy, from the case 1 to case 2 and 3, may well pose the concern as to the applicability of the Wyllie acoustic model to predict the acoustic velocity in fractured vuggy carbonate rocks, such as the Tahe Ordovician carbonates. But, it has been argued that the Wyllie model can be applied to derive reasonable porosity estimate by inverting the rock-bulk velocity in the presence of monophasic pore type, i.e. intercrystalline and interparticle porosity (Anselmetti and Eberli, 1999; Saleh and Castagna, 2004). It is, therefore, suggested that the present improved accuracy in the porosity prediction using the Wyllie acoustic model may partly result from the determination of the effective rock matrix properties through multi-mineral analysis. However, the assumption of constant interval transit time and neutron content for the fluid phase for continuous depth, which may not necessarily be accurate, could have adversely affected the accuracy of the results.

On the other hand, the results show how the generalized Wyllie acoustic model can enable a more satisfactory vuggy porosity estimation using the velocity–porosity relation. This is because the generalized Wyllie acoustic model can enable to account for the variations of pore structure types, which, in addition to the rock mineral composition and pore fluid types, condition the rock elastic properties and influence strongly the velocity–porosity relationship in carbonate rocks (Saleh and Castagna, 2004; Sun, 2004; Dou et al., 2011; Huang et al., 2017; Jin et al., 2017). This point is implicitly stressed by the introduction of the pore shape factor (s) that, varying with the nature and abundance of the pore type, explicitly quantifies the influence of pore structure types on

the velocity–porosity relationship (Saleh and Castagna, 2004; Sun, 2004). Similarly, several studies have demonstrated that pore-size distribution and pore geometrical parameters are key factors controlling the variations of physical properties in carbonate rocks (e.g. Anselmetti and Eberli, 1993; Anselmetti et al., 1998; Clerke et al., 2008; Weger et al., 2009; Archilha et al., 2016; Fournier et al., 2018; Cilli and Chapman, 2020).

The integration of multi-techniques, such as rock-physics modeling, and digital image analysis, using multi-scale data has been used to characterize carbonate reservoirs in many studies. Recently, Sun et al. (2019), through multi-scale digital rock imaging, have investigated the pore system heterogeneity and its influence on physical properties and have suggested that averaging the image-derived estimates can be an affordable upscaling approach. Oliveira et al. (2020) conducted 2D/3D digital image analyses to quantify the porosity in terms of macroporosity and microporosity to determine their influence on the porosity-permeability relationship, and to demonstrate how the permeability is sensitive to the pore-shape parameters. They have processed the thin-section micrographs comparably to this study. However, the existing image analysis methods provide in general single-point estimates that are extrapolated to establish continuous profiles (Valentín et al., 2018); additionally, the total porosity is derived from core analysis and standard porosity logs, and ithis does not necessarily make a good approximation in carbonates characterized by multimodal porosity of varying sizes.

This paper has discussed an approach developed to determine and portion total porosity into fractions of its components and establish vuggy porosity models by use of the rock-physics models and image analysis techniques based on multi-scale data integration. The log-derived total and effective porosity compare well and fairly good with the thin-section optical porosity (PHIO) and corrected core porosity, respectively. The statistical assessment of the regression results shows that the models that relate the vug fractions to acoustic intercepts linearly enable a robust vuggy porosity modeling, particularly the models

M233 and M333. Typical models are as follows:

$$\varphi_v = A + Blog(C),\tag{9a}$$

$$C = \left[\Delta t_l - \left(\Delta t_f - \Delta t_{ma}^s\right)\varphi\right]^{\frac{1}{s}} \quad or \quad C = \left[\left(\Delta t_l - \varphi\Delta t_f\right)/(1-\varphi)\right]^{\frac{1}{s}}\tag{9b}$$

where φ is the total porosity derived applying the present procedure, and it can be substituted for the porosity derived from standard total porosity logs, in this study, the density log, in the model, and the pore-shape factor equation to predict separate vug porosity.

At this point, considering that the present approach made use of the core and standard and image logging data, there appears the necessity to explore other sound means applicable to derive reliable total porosity estimates by use of the conventional well logs only. It can allow the application of the total vuggy-porosity model in wells without core data or image logs. It is because, in an economic sense, it is impractical to core an entire well or run FMI log on every single drilled-well considering the prohibiting cost, in addition to the immense technical challenges related to coring in carbonates (Yarmohammadi et al., 2020).

5. Conclusion

In the studied oilfield, the evaluation of reservoir porosity has been challenging because the pore system is complex and composed mostly of secondary reservoir space types, including solution-enlarged fractures, vugs, molds, and caves. These pore types could not readily be resolved by independently using routine core analysis and standard logging methods.

A new approach is developed by integrating standard and advanced logging methods to decompose the determined total porosity into fractions of its components. The validity of the newly-proposed procedure to estimate and portion the total porosity is demonstrated by comparing the log-derived total and effective porosity to the (2D) thin-section optical porosity (PHIO), and the corrected effective porosity measured from the full-diameter core, respectively. The results show there is a good match between the log-derived total porosity and 2D PHIO, and a reasonable match between the log effective porosity and the corrected core effective porosity, respectively.

The statistical evaluation demonstrates that the vuggy porosity models established using the acoustic intercept equations modified from the generalized Wyllie acoustic model show better modeling accuracy. Plotting the acoustic intercept along the *x*-axis in log-value and the

vuggy porosity along the *y*-axis in normal value enables to define more consistent velocity–vuggy porosity relationships. This implies the models M233 and M333 are to preferably be applied to model the total-vug and separate-vug porosities.

The development of the present approach requires clear prior knowledge of the lithology (rock matrix), pore fluid types, pore type composition, and elastic and density properties of the bulk rock, constituent minerals, and pore fluids. The results obtained may support the application of this approach in typical carbonate reservoirs; its contribution to ensure accurate determination of reservoir physical properties such as water saturation and permeability is discussed in future works.

CRediT authorship contribution statement

Issoufou Aboubacar Mahaman Salifou: Conceptualization, Methodology, Formal analysis, Validation, Investigation, Data curation, Writing - original draft. **Heng Zhang:** Conceptualization, Methodology. **Issoufou Ousmane Boukari:** Conceptualization. **Moussa Harouna:** Formal analysis, Writing - review & editing. **Zhongxian Cai:** Project administration, Investigation, Validation.

Declaration of competing interest

The authors declare that they have no known competing financial interests or personal relationships that could have appeared to influence the work reported in this paper.

Appendix A. Multi-mineral analysis and porosity determination using conventional logs

The true matrix properties are established based on the computation of the rock volumetric mixture. The fractional volume of each solid rock component is first obtained in a fraction of the total rock volume and then normalized following the truism that the relative fractions would sum to unity. The weighted average matrix properties, such as density (ρ), and slowness (Δt), are calculated using Eq. (A.1a) through Eq. (A.1c); the weights are the mineral volume fractions. Thus, it is established the true matrix properties variable with the rock composition rather than constant zero-porosity values. Moreover, the approach has also provided the porosity estimate, referred hereinafter as virtual porosity, and fluid saturation estimates, etc. As usual, the accuracy of mineral volume computation is verified based on a resolution number,]4–6[, which, in this case, ~ 3.93, which is obtained by iteratively adjusting the log-response characteristic values related to the different mineral components through trial and error until the model is accurate enough (Table A1).

$$X_T = \sum_{i=1}^{n} V_{ni}X_{H_i} \, ,\tag{A.1a}$$

where

$$V_{ni} = \frac{V_i}{1-\varphi} \, ,\tag{A.1b}$$

and

$$\sum_{i=1}^{n} V_{ni} = 1 \ , \tag{A.1c}$$

where X_T represents a given true matrix property parameter; V_i and V_{ni} are the computed and normalized volume fraction of a given solid formation component, respectively. X_{Hi} is the hypothetical tool response for each pure mineral component (homogeneous mineral component i), and φ is the modeled "virtual" porosity. The model parameters used for the determination of the true matrix properties and porosity are presented in Table A2.

Table A.1

1. Parameters used in the multi-mineral analysis; 2. Parameters used in the calculation of true matrix properties and porosities, (Tixier and Alger, 1970; Raymer et al., 1980; Etnyre, 1989; Hashmy and Alberty, 1998).

MINERAL	DEN	GR	CNL	AC
Clay	2.48	200	32	88
Dolomite	2.87	29	1	42
Limestone	2.71	50	−1	47.5
Formation Fluid	1	0	100	189
				1

MINERAL	DEN	CNL	AC
Clay	2.48	32	88
Dolomite	2.87	1	44
Limestone	2.71	−1	49
			2
Fluid	variable	100	185

Additionally, the shale volume is calculated from the gamma-ray log applying the Clavier's model (Asquith and Krygowski, 2004) using Eq. (A.2a) and (A.2 b). Throughout the logged intervals, the values obtained are in general very small, < 4%, and it can indicate that the formations are relatively clean and pure carbonates, which agrees with the core-thin section petrography results. Thus, it is assumed that the presence of shale is herein effectless on the rock physical properties, and the shale effect correction appears to be unnecessary (Hilchie, 1978).

$$V_{sh} = 1.7 \times \left(3.38 - \left(I_{GR} - 0.7\right)^2\right)^{\frac{1}{2}} , \tag{A.2a}$$

$$I_{GR} = \frac{GR_l - GR_{min}}{GR_{max} - GR_{min}} , \tag{A.2b}$$

where V_{sh} is the shale content; I_{GR} = gamma ray index, GR_l = gamma ray from log at a specific formation depth, and GR_{max} and GR_{min} are the maximum and the minimum gamma ray, respectively.

Next, with the availability of the true matrix properties, the density and neutron logs are inverted to derive the density porosity and neutron porosity, respectively, using Eq. (A.3) and (A.4). These porosities are then combined to calculate the neutron-density porosity, commonly referred to as total porosity, using Eq. (A.5). Because carbonates usually show advanced pore system complexity, CNL-FDC porosity can generally represent the total porosity for sand-shale reservoir formations, however (Aïfa et al., 2014). Therefore, the CNL log may not provide a good porosity estimate throughout the logged interval. It is because the neutron log responds primarily to hydrogen content and that the studied formations contain gas, oil, and water. As a result, it is suggested that the neutron log measurement may not reliably indicate the total porosity, compared with the density log. It is because the density log responds to the formation electronic density, which is, in turn, varies with the density of the rock matrix and pore-saturating fluids, and the porosity itself. Additionally, the borehole is relatively stable to ensure high quality density measurements. Next, the matrix porosity, commonly referred to as interparticle/primary porosity, is derived from the acoustic interval transit time by applying the Wyllie porosity-transform using Eq. (A.6).

$$\varphi_D = \frac{\rho_{ma} - \rho_b}{\rho_{ma} - \rho_f}, \tag{A.3}$$

$$\varphi_N = \frac{CNL_{ma} - CNL_b}{CNL_{ma} - CNL_f} , \tag{A.4}$$

$$\varphi_{ND} = \frac{1}{3}\varphi_N + \frac{2}{3}\varphi_D , \tag{A.5}$$

$$\varphi_m = \frac{\Delta t_l - \Delta t_{ma}}{\Delta t_f - \Delta t_{ma}} , \tag{A.6}$$

where ρ, Δt and CNL are the density, slowness, and neutron values, respectively, and expressed in gram per cubic centimeter (g/cm^3), microseconds per feet (μs/ft), and percentage (%), respectively; the subscripts b, f and ma refer to the bulk, matrix, and fluid component.

It has been argued that the porosity inversion results from the aforementioned standard porosity logs may rarely meet expectations (Hurley et al., 1998; Perrin et al., 2007). It is because these logs are characterized by a poor vertical resolution related to the sampling rate and tools' poor intrinsic resolution, a critical limitation to their application for carbonates, in addition to the complexity of carbonate pore systems (Masoudi et al., 2018). Thus, a reliable carbonate pore system examination requires the use of high-resolution data such as image logs and digital rock physics data, which can enable a clearer observation of rock internal organizations, namely about the rock textures and structures (Mehmani et al., 2019). However, integrated well-log data upon calibration with high-resolution data can possibly provide more reliable and complete knowledge of pore properties (Sun, 2000). Such integration is attempted in the present investigation to cope with the complexities of pore structures in the study oilfield.

Fracture porosity determination: The fracture judging index (Y) allows the identification of the fracture type through the determination of fracture

dip-angle (Deng et al., 2006), and the selection of appropriate values for the different A constants according to the calculated values of Y. The calculation equations are as follows:

$$\varphi_f = \left(\frac{A_1}{R_S} + \frac{A_2}{R_D} + A_3\right) \times R_{mf} ,$$
(A.7a)

$$Y = \frac{R_D - R_S}{\sqrt{R_D \times R_S}} ,$$
(A.7b)

where φ_f is the fracture porosity, R_S, R_D and R_{mf} are the shallow (LLS), deep (LLD) Laterolog, and mud filtrate resistivity in Ω.m, respectively, and A_1, A_2 and A_3 are constants varying with the fracture type or the Y parameter (dimensionless) called the fracture discriminating index.

Table A.2
The fracture judging parameter Y and constants used in fracture porosity calculation (Li et al., 1996; Deng et al., 2006)

Y	FRACTURE TYPE	A$_1$	A$_2$	A$_3$
$Y < 0$	Low-angle fracture	-0.992417	1.97247	0.000318291
$0 \leq Y \leq 0.1$	Dipping fracture	-17.6332	20.36451	0.00093177
$Y > 0.1$	High-angle fracture	8.522532	-8.242788	0.00071236

The model in Eq. (A.7a) clearly shows that accurate R_{mf} values are necessary to ensure accurate fracture porosity estimation. We herein derive realistic R_{mf} estimate based on the actual measured mud resistivity (R_m) and density (ρ_m) data by applying the Overton and Lipson (1958) correlation, $R_{mf} = K(R_m)^{1.07}$, where the empirical factor K is mud weight dependent. By crossplotting the data in the table appearing in Schlumberger book chart, Gen-3 (Schlumberger, 2009), it is observed that the variation of K with the mud density can be better predicted using a power-law equation, $K = 1.0474\,(\rho_m)^{-1.556}$ and $R^2 = 0.94$, which is further applied to determine K using the measured mud weights. The drilling mud resistivity and density are 0.282 Ω m and 1.13 g/cm^3, respectively, and 1.02 Ω m and 1.13 g/cm^3, respectively, taken at 24 °C in Wells A and B, respectively. The resistivity conversion to formation temperature is carried out using Arps's formula for temperatures in degree Celsius (Arps, 1953), and the formation temperature is determined using Eq. (A.8).

$$T_f = \Delta T \times D_f + T_s ,$$
(A.8)

where T_f is the formation temperature, D_f is the formation depth (continuous), T_S is the mean local monthly surface temperature taken as -8.3 °C and $+32.4$ °C for January and October, respectively (Fu et al., 2003), at the logging time for Wells A and B, respectively, and the geothermal gradient ΔT is assumed to be 21.5 °C/km (Feng et al., 2009).

Appendix B. Acquisition of digital thin-section image (micrographs)

The impregnation of the thin-section porosity with blue dyed resin allows the visualization of the pore types. The thin-section observation is performed using a Zeiss Axio Imager A2 microscope. We have used EC-Epiplan-NEOFLUAR (5X/0.16, ∞/0.17) objective lens which allows achieving sharp Circular Differential Interference Contrast (C-DIC) and a flat, in focus, 25 mm field of view. Such characteristics permit a detailed description of the rock microstructures and textures from the thin-section images. The microscope is connected to a PC computer, and the micrographs (JPEG file) are captured using a CamWare software camera set at a resolution of 2404 × 1994 pixels (pixel depth = 24 bits), and under plane polarized light. For each thin-section, as many micrographs as necessary (N > 15) and possibly the entire section image, were collected to avoid some sampling bias (volume representativeness) and scaling concern.

NO	EQUATION	VARIABLE	ROCK TEXTURE	PORE STRUCTURE	AUTHOR (S)
1	$\varphi_2 = \varphi_t - \varphi_S$	φ_t, φ_s	Carbonates	IP, FR, VUG	Schlumberger (1974)
2	$\varphi_{sv} = \dfrac{m - 1.9}{2.2} \times \varphi$	m, φ (φ_{ND})	Limestone	IP, SV	Lucia (1983)
3	$\varphi_{om} = 2(\varphi_t - \varphi_S)$	φ_t, φ_s	Limestone	IP, SV-MO	Nurmi (1984)
4	$\varphi_S = \dfrac{\varphi_t - \varphi_m}{1 - \varphi_m}$	φ_t, φ_m	Limestone	IP, VUG	Brie et al. (1985)
5	$\varphi_{sv} = 10^{4.09 + 0.1298\,(\Delta t - 141.5\varphi)}$	$\varphi_{ND}, \Delta t$	Limestone	IP, SV	Lucia and Conti (1987)
6	$\varphi_{sv} = 10^{4.4419 + 0.1529\,(\Delta t - 141.5\varphi)}$	$\varphi_{ND}, \Delta t$	Anhydritic Dolomite	IP, SV	Lucia (1991)
7	$\varphi_{SV} = (\varphi_t - \varphi_S) + p(\varphi_t - \varphi_S)^2$	p, φ_{ND}, φ_t,	–	IP, SV-MO	Wang and Lucia (1993)
8	$\varphi_{SV} = (\varphi_t - \varphi_S)\,(\varphi_t/\varphi_S)^\alpha$	p, φ_{ND}, φ_t	–	IP, SV-MO	Wang and Lucia (1993)
9	$\varphi_S = \dfrac{\varphi - \varphi_h}{1 - \varphi_h}$	φ, φ_h	Carbonates	IG, VUG	Ramamoorthy et al. (1999)
10	$\varphi = \sqrt{\dfrac{R_{mf}}{R_{xo}}}$	R_{mf}, R_{xo}	Carbonates	IG, VUG	Newberry et al. (1996)
11	$\varphi_{im} = PXND\sqrt{\dfrac{LLS}{R_i}}$	PXND, LLS, Ri	Dolomite	IP, WP, VUG	Xu et al. (2006)
12	$\varphi_{SV} = \varphi_t + (1/F)^{\frac{1}{m}}$	Φ_t, F, m	Carbonates	IP, SV	Müller-Huber and Schön, 2013
13	$\sigma_{prdiff} = (\sum_{i=m_f}^n P_{\varphi_i}(\varphi_i - \varphi_{m_f})^2)/(\sum_{i=m_f}^n P_{\varphi_i})$	Pφi, mf, φi, φ_{mf}	Reef-bank Carbonates	IP, VUG	Fu et al. (2016)

Note: FR = fracture; IG = intergrain pore; IP = interparticle pore; MO = moldic pore; SV = separate vugs; VUG = vugs (separate and touching); and WP = intraparticle pore. For a variable, refer to the related literature.

Appendix C. Supplementary data

Supplementary data to this article can be found online at https://doi.org/10.1016/j.petrol.2020.107700.

References

Aïfa, T., Baouche, R., Baddari, K., 2014. Neuro-fuzzy system to predict permeability and porosity from well log data: a case study of Hassi R'Mel gas field, Algeria. J. Petrol. Sci. Eng. 123, 217–229. https://doi.org/10.1016/j.petrol.2014.09.019, 2014.

Akbar, M., Petricola, M., Watfa, M., et al., 1995. Classic interpretation problems: evaluating carbonates. Oilfield Rev. 7, 38–57.

Andrä, H., Combaret, N., Dvorkin, J., et al., 2013. Digital rock physics benchmarks—Part II: computing effective properties. Comput. Geosci. 50 (January), 33–43. https://doi.org/10.1016/j.cageo.2012.09.008.

Anselmetti, F.S., Eberli, G.P., 1993. Controls on sonic velocity in carbonates. Pure Appl. Geophys. 141 (2–3-4), 287–323.

Anselmetti, F.S., Luthi, S., Eberli, G.P., 1998. Quantitative characterization of carbonate pore systems by digital image analysis. AAPG Bull. 82 (10), 1815–1836.

Anselmetti, F.S., Eberli, G.P., 1999. Velocity deviation log: a tool to predict pore type and permeability trends in carbonate drill holes from sonic and porosity or density logs. AAPG Bull. 83 (3), 450–466.

Archilha, N.L.R.M., Missagia, C., Hollis, M.A., et al., 2016. Permeability and acoustic velocity controlling factors determined from x-ray tomography images of carbonate rocks. AAPG Bull. 100 (8), 1289–1309. https://doi.org/10.1306/02251615044.

Arps, J.J., 1953. The effect of temperature on the electrical resistivity of sodium chloride solutions. J. Petrol. Technol. 5 (10), 17–20. SPE-953327-G. https://dx./doi.org/10.2118/953327-G.

Asquith, G., Krygowski, D., 2004. Basic Well Log Analysis, second ed., vol. 16. AAPG Methods in Exploration, pp. 31–35.

Bahrami, F., Moussavi-Harami, R., Khanehbad, M., et al., 2017. Identification of pore types and pore facies for evaluating the diagenetic performance on reservoir quality: a case study from the Asmari Formation in Ramin Oil Field, SW Iran. Geosci. J. 21 (4), 565–577. https://doi.org/10.1007/s12303-016-0014-0.

Barton, C.A., Zoback, M.D., 2002. Wellbore imaging technologies applied to reservoir geomechanics and environmental engineering. In: Lovell, M., Parkinson, N. (Eds.), Geological Applications of Well Logs, vol. 13. AAPG Methods in Exploration, pp. 229–239.

Baqués, V., Ukar, E., Laubach, S.E., et al., 2020. Fracture, Dissolution, and Cementation Events in Ordovician Carbonate Reservoirs, Tarim Basin, NW China. Geofluids, Special Issue. https://doi.org/10.1155/2020/9037429. Accepted.

Bayuk, I.O., Dubinya, N.V., Garagash, I.A., et al., 2019. Multiscale rock-physics modeling of effective elastic properties of fractured reservoir rocks. In: Presented at the 53rd US Rock Mechanics/Geomechanics Symposium, New York, 23–26 June. ARMA 19–415.

Boyeldieu, C., Winchester, A., 1982. Use of the dual laterolog for the evaluation of the fracture porosity in hard carbonate fonnations. In: Presented at the Offshore South East Asia 82 Conference, Singapore, 9–12 February. SPE-10464-MS https://dx.doi.org/doi:10.2118/10464-MS.

Brie, A., Johnson, D.L., Nurmi, R., 1985. Effect of spherical pores on sonic and resistivity measurements. In: Paper W Presented at the Transactions of SPWLA 26th Annual Logging Symposium, Dallas, Texas, 17–20 June. SPWLA-1985-W.

Buono, A., Fullmer, S., Luck, K., et al., 2019. Quantitative digital petrography: full thin section quantification of pore space and grains. In: Presented at the SPE Middle East Oil and Gas Show and Conference, Manama, Bahrain, 18–21 March. SPE-194899-MS. https://doi.org/10.2118/194899-MS.

Chai, H., Li, N., Xiao, C., et al., 2009. Automatic discrimination of sedimentary facies and lithologies in reef-bank reservoirs using borehole image logs. Appl. Geophys. 6 (1), 17–29. https://doi.org/10.1007/s11770-009-0011-4.

Choquette, P.W., Pray, L.C., 1970. Geologic nomenclature and classification of porosity in sedimentary carbonates. AAPG Bull. 54 (2), 207–250.

Cilli, P.A., Chapman, M., 2020. The power-law relation between inclusion aspect ratio and porosity: implications for electrical and elastic modeling. J. Geophys. Res.: Solid Earth 125, e2019JB019187. https://doi.org/10.1029/2019JB019187.

Clerke, E.A., Mueller III, H.W., Phillips, E.C., et al., 2008. Application of thomeer hyperbolas to decode the pore systems, facies and reservoir properties of the upper jurassic arab D limestone, ghawar field, Saudi arabia: a "rosetta stone" approach. GeoArabia 13 (4), 113–160.

Cunningham, K.J., Carlson, J.I., Hurley, N.F., 2004. New method for quantification of vuggy porosity from digital optical borehole images as applied to the karstic Pleistocene Limestone of the Biscayne Aquifer, Southeastern Florida. J. Appl. Geophys. 55 (1–2), 77–90 https://doi.org/10.1016/j.jappgeo.2003.08.003.

Dehghani, K., Harris, P.M., Edwards, K.A., et al., 1999. Modeling a vuggy carbonate reservoir, McElroy Field, West Texas. AAPG Bull. 83 (1), 19–42.

Delhomme, J.P., 1992. A quantitative characterization of formation heterogeneities based on borehole image analysis. In: Paper T Presented at the SPWLA 33rd Annual Logging Symposium, Oklahoma City, Oklahoma, 14–17 June. SPWLA-1992-T.

Deng, S.G., Wang, X.C., Zou, D.J., et al., 2006. Interpreting dual laterolog fracture data in fractured carbonate formation. J. China Univ. Geosci. 17 (2), 168–172. https://doi.org/10.1016/s1002-0705(06)60024-1.

Ding, W., Fan, T., Yu, B., et al., 2012. Ordovician carbonate reservoir fracture characteristics and fracture distribution forecasting in the Tazhong Area of Tarim Basin, Northwest China. J. Petrol. Sci. Eng. 86–87 (May), 62–70. https://doi.org/10.1016/j.petrol.2012.03.006.

Ding, Z., Wang, R., Chen, F., et al., 2020. Origin, hydrocarbon accumulation and oil-gas enrichment of fault-karst carbonate reservoirs: a case study of Ordovician carbonate reservoirs in South Tahe area of Halahatang oilfield. Tarim Basin. Petrol. Explor. Develop 47 (2), 306–317. https://doi.org/10.1016/S1876-3804(20)60048-9.

Dou, Q., Sun, Y., Sullivan, C., 2011. Rock-physics-based carbonate pore type characterization and reservoir permeability heterogeneity evaluation, Upper San Andres Reservoir, Permian basin, West Texas. J. Appl. Geophys. 74 (1), 8–18. https://doi.org/10.1016/j.jappgeo.2011.02.010.

Etnyre, L.M., 1989. Finding Oil and Gas from Well Logs. Springer Science+Business Media, New York, p. 312.

Farooq, U., Ahmed, J., Ali, S., et al., 2019. Heterogeneity in the petrophysical properties of carbonate reservoirs in Tal Block. In: Paper F Presented at SPWLA 60th Annual Logging Symposium, Woodlands, Texas, 17–19 June. SPWLA-2019_F. https://doi.org/10.30632/T60ALS-2019_F.

Feng, C.G., Liu, S.W., Wang, L.S., et al., 2009. Present-day geothermal regime in Tarim Basin, northwest China: Chinese. J. Geophys. 52 (6), 1237–1250. https://doi.org/10.1002/cjg2.1450.

Fournier, F., Pellerin, M., Villeneuve, Q., et al., 2018. The equivalent pore aspect ratio as a tool for pore type prediction in carbonate reservoirs. AAPG Bull. 102 (7), 1343–1377. https://doi.org/10.1306/10181717058.

Fu, H., Zou, C., Li, N., et al., 2016. A quantitative approach to characterize porosity structure from borehole electrical image and its application in a carbonate reservoir in the Tazhong Area, Tarim Basin. SPE Reservoir Eval. Eng. 19 (1), 18–23. https://doi.org/10.2118/179719-PA. SPE-179719-PA.

Fowler, M.L., Johnson, W.I., Safley, L.E., et al., 1999. Field Demonstrations of Logging Technologies for Reservoir Characterization. National Petroleum Technology Office. U.S. Department Of Energy Tulsa, Oklahoma. DOE/PC/91008-0379 (OSTI ID: 3332).

Fu, W.D., Wang, J., Liu, S.M., 2003. Studies on the distribution rule of ground temperatures in Tarim Oilfield. J. Arid Land Resour. Environ. 17 (6), 99–102.

Gaymard, R., Poupon, A., 1968. Response of neutron and formation density logs in hydrocarbon bearing formations. Log. Anal. 3–12. SPWLA-1968-VIXN5A1.

Genty, C., Jensen, J.L., Ahr, W.M., 2007. Distinguishing carbonate reservoir pore facies with nuclear magnetic resonance measurements. Nat. Resour. Res. 16 (1), 45–54. https://doi.org/10.1007/s11053-007-9035-8.

Ghadami, N., Rasaei, M.R., Hejri, S., et al., 2015. Consistent porosity–permeability modeling, reservoir rock typing and hydraulic flow unitization in a giant carbonate reservoir. J. Petrol. Sci. Eng. 131 (July), 58–69. https://doi.org/10.1016/j.petrol.2015.04.017.

Ghafoori, M.R., Roostaeian, M., Sajjadian, V.A., 2009. Secondary porosity: a key parameter controlling the hydrocarbon production in heterogeneous carbonate reservoirs (case study). Petrophysics 50 (1), 67–78. SPWLA-2009-V50N1A4.

Guo, C., Chen, D., Qing, H., et al., 2016. Multiple dolomitization and later hydrothermal alteration on the upper cambrian-lower ordovician carbonates in the northern Tarim Basin, China. Mar. Petrol. Geol. 72 (April), 295–316. https://doi.org/10.1016/j.marpetgeo.2016.01.023.

Hashmy, K., Alberty, M., 1998. Log Analysis, Lithology. 30 January 2014, wiki.aapg.Org. (Accessed 6 March 2018).

Hassan, A., Chandra, V., Yutkin, M.P., et al., 2019. Imaging and characterization of microporous carbonates using confocal and electron microscopy of epoxy pore casts. SPE J. 24 (3), 1220–1233. https://doi.org/10.2118/188786-PA. SPE-10.2118/188786-PA.

Hilchie, D.W., 1978. Applied Openhole Log Interpretation: Golden. Colorado. D.W. Hilchie. Inc.

Huang, Q., Dou, Q., Sun, Y., 2017. Characterization of pore structure variation and permeability heterogeneity in carbonate rocks using MICP and sonic logs: puguang Gas Field, China. Petrophysics 58 (6), 576–591. SPWLA-2017-V58N6A2.

Hurley, N.F., Zimmerman, R.A., Pantoja, D., 1998. Quantification of vuggy porosity in a dolomite reservoir from borehole images and core, Dagger Draw Field. In: New Mexico. Presented at the SPE Annual Technical Conference and Exhibition, New Orleans, Louisiana, 27–30 September. SPE-49323-MS. https://dx.doi.org/10.2118/49323-MS.

Ijasan, O., Torres-Verdin, C., Preeg, W.E., 2013. Interpretation of porosity and fluid constituents from well logs using an interactive neutron-density matrix scale. Interpretation 1 (2), T143–T155. https://doi.org/10.1190/INT-2013-0072.1.

Inês, N., Bizarro, P., Ribeiro, T., 2015. Integrated carbonate reservoir characterization and modelling with depositional and diagenetic trends. In: Presented at the SPE Reservoir Characterization and Simulation Conference and Exhibition, Abu Dhabi, 14–16 September. SPE-175673-MS. https://doi.org/10.2118/175673-MS.

Jacobsen, S., Everett, B., Levien, L., et al., 1990. Log interpretation strategies in gas wells. In: Presented at the SPWLA 31st Annual Logging Symposium (Discussion) Lafayette, Louisiana, 24–27 June.

Jin, X., Dou, Q., Hou, J., et al., 2017. Rock-physics-model-based pore type characterization and its implication for porosity and permeability qualification in a deeply-buried carbonate reservoir, Changxing Formation, Lower Permian, Sichuan Bain, China. J. Petrol. Sci. Eng. 153 (May), 223–233. https://doi.org/10.1016/j.petrol.2017.02.003.

Jin, Z., Zhu, D., Hu, W., et al., 2009. Mesogenetic dissolution of the Middle ordovician limestone in the Tahe oilfield of Tarim Basin, NW China. Mar. Petrol. Geol. 26 (6), 753–763 https://dx.doi.org/1 0.1016/j.marpetgeo.2008.08.005.

Jonathan Soto, O., David Soto, O., Rodolfo Soto, O., 2015. A new reservoir classification based on pore types improves characterization – Part B. In: Presented at the SPE Latin American and Carribbean Petroleum Engineering Conference, Quito, Ecuador, 18–20 November. SPE-117237-MS https://dx.doi.org/10.2118.117237-MS.

Kuster, G.T., Toksöz, M.N., 1974. Velocity and attenuation of seismic waves in two-phase media – Part I, theoretical formulations. Geophysics 39 (5), 587–606. https://doi.org/10.1190/1.1440450.

Li, S., Xiao, C., Wang, H., et al., 1996. Mathematical model of dual laterolog response to fracture and quantitative interpretation of fracture porosity. Acta Geophysica Sinica 39 (6), 845–852 (in Chinese with English Abstract).

Li, Y., Hou, J., Ma, X., 2016. Data integration in characterizing a fracture-cavity reservoir, Tahe oilfield, Tarim Basin, China. Arab J Geosci 9 (8), 532–543. https://doi.org/10.1007/s12517-016-2562-z.

Li, B., Tan, X., Wang, F., et al., 2017. Fracture and vug characterization and carbonate rock type automatic classification using X-ray CT images. J. Petrol. Sci. Eng. 153 (May), 88–96. https://doi.org/10.1016/j.petrol.2017.03.037.

Li, H., Zhang, J., 2018. Well log and seismic data analysis for complex pore-structure carbonate reservoir using 3D rock physics templates. J. Appl. Geophys. 151 (April), 175–183. https://doi.org/10.1016/j.jappgeo.2018.02.017.

Liu, L.H., Ma, Y.S., Liu, B., et al., 2017. Hydrothermal dissolution of Ordovician carbonates rocks and its dissolution mechanism in Tarim Basin, China. Carbonates Evaporites 32 (4), 525–537. https://doi.org/10.1007/s13146-016-0309-2.

Lønøy, A., 2006. Making sense of carbonate pore systems. AAPG Bull. 90 (9), 1381–1405. https://doi.org/10.1306/03130605104.

Lucia, F.J., 1983. Petrophysical parameters estimated from visual descriptions of carbonate rocks: a field classification of carbonate pore space. J. Petrol. Technol. 35 (3), 629–637. https://doi.org/10.2118/10.2118/10073-PA, 10073-PA.

Lucia, J.F., 1991. Geological engineering aspects of the san andres reservoirs in the lawyer canyon, algerita escarpment outcrop and seminole, subsurface field. In: Kerans, C., Lucia, F.J., Senger, R.K., Fogg, G.E., Nance, H.S., Kasap, E., Hovorka, S.D. (Eds.), Characterization of Reservoir Heterogeneity in Carbonate-Ramp Systems, San Andres/Grayburg, Permian Basin, 11 7. The University of Texas at Austin, Bureau of Economic Geology, final report prepared by Reservoir Characterization Research Laboratory, pp. 1–74.

Lucia, F.J., 1995. Rock-fabric/petrophysical classification of carbonate pore space for reservoir characterization. AAPG Bull. 79 (9), 1275–1300 https://dx.doi.org/10.1306@7834d4a4-1721-11d7-8645000102c1865d.

Lucia, F.J., 2007. Carbonate Reservoir Characterization: an Integrated Approach. Springer Verlag, Berlin.

Lucia, F.J., Conti, R.D., 1987. Rock fabric, permeability, and log relationships in an upward-shoaling, vuggy carbonate sequence. University of Texas at Austin, Bureau of Economic Geology. Geological Circular 87–5, pp22.

Malik, S., Sharma, R., 2019. Feasibility of digital rock physics for static and dynamic reservoir property characterization in carbonate reservoirs-I. In: Paper QQQQ Presented at the SPWLA 60th Annual Logging Symposium, Woodlands, Texas, 17–19 June. https://doi.org/10.30632/T60ALS-2019_QQQQ. SPWLA-2019-QQQQ.

Masoudi, P., Aïfa, T., Memarian, H., et al., 2018. Uncertainty assessment of porosity and permeability by clustering algorithm and fuzzy arithmetic. J. Petrol. Sci. Eng. 161, 275–290. https://doi.org/10.1016/j.petrol.2017.11.018, 2018.

Mavko, G., Mukerji, T., 1995. Seismic pore space compressibility and gassmann's relation. Geophysics 60 (6), 1743–1749. https://doi.org/10.1190/1.1443907.

Meese, A.D., Walther, H.C., 1967. An investigation of sonic velocities in vugular carbonates. In: Paper P Presented at the SPWLA 8th Annual Logging Symposium, Denver, 12–14 June. SPWLA-1967-P.

Mehmani, A., Kelly, S., Torres-Verdín, C., 2019. Leveraging digital rock physics workflows in unconventional petrophysics: a review of opportunities, challenges, and benchmarking. In: Paper CCCC Presented at the SPWLA 60th Annual Logging Symposium, Woodlands, Texas, 17–19 June. SPWLA-2019-CCCC. https://doi.org/10.30632/T60ALS 2019_CCCC.

Meng, M., Fan, T., Duncan, I.J., et al., 2018. Characterization of carbonate microfacies and reservoir pore types based on formation microimager logging: a case study from the Ordovician in the Tahe Oilfield, Tarim Basin, China. Interpretation 6 (1), T71–T82. https://doi.org/10.1190/INT-2017-0043.1.

Merza Media, A., Muhajir, M.M., Wahdanadi, H., et al., 2019. Novel workflow to characterize secondary porosity in carbonate reservoir, case study of tuban formation-Indonesia. In: Presented at the International Petroleum Technology Conference, Beijing, 26–28 March. IPTC-19409-MS. https://doi.org/10.2523/IPTC-19409-MS.

Mollajan, A., Memarian, H., 2016. Rock physics-based carbonate pore type identification using parzen classifier. J. Petrol. Sci. 145 (September), 205–212 https://dx.doi.org/10.1016/j.petrol.2016.03.021.

Mousavi, M.A., Prodanovic, M., Jacobi, D., 2012. New classification of carbonate rocks for process-based pore-scale modeling. SPE J. 18 (2), 243–263. https://doi.org/10.2118/163073-PA. SPE-163073-PA.

Müller-Huber, E., Schön, J., 2013. A modified Archie relationship-a novel approach to evaluate carbonate reservoirs with regard to fracture and isolated vuggy porosity for Sw = 1. In: Presented at the International Petroleum Technology Conference, Beijing, 26–28 March. IPTC-16695-MS https://dx.doi.org/10.2523/IPTC-16695-MS.

Newberry, B.M., Grace, L.M., Stief, D.D., 1996. Analysis of carbonate dual porosity systems from borehole electrical images. In: Presented at the Permian Basin Oil and Gas Recovery Conference, Midland, Texas, 27–29 March. SPE-35158-MS. https://doi.org/10.2118/35158-MS.

Ning, C.Z., 2017. Control of stratigraphic sequence on karst reservoirs: a case study on the reservoirs in the North Tarim Basin, China. In: Presented at the AAPG Annual Convention and Exhibition, Houston, Texas, 2–5 April. Search and Discovery Article #10936.

Nurmi, R.D., 1984. Carbonate pore systems: porosity/permeability relationships and geological analysis (abs.). AAPG Bull. 68, 513–514.

Oliveira, G.L.P., Ceia, M.A.R., Missagia, R.M., et al., 2020. Core plug and 2D/3D-image integrated analysis for improving permeability estimation based on the differences between micro- and macroporosity in Middle East carbonate rocks, 2020 J. Petrol. Sci. Eng. 193, 107335. https://doi.org/10.1016/j.petrol.2020.107335, 1–13.

Overton, H.L., Lipson, L.B., 1958. A correlation of the electrical properties of drilling fluids with solids content. SPE Pet Trans 213, 333–336. SPE-1171-G. https://dx.doi.org/10/2118/1171-G.

Pérez-Rosales, C., Luna, L., 2004. Characterization of vuggy fractured media: a practical approach. In: Presented at the SPE International Petroleum Engineering Conference, Puebla, Mexico, 8–9 November. SPE-91863-MS. https://doi.org/10.2118/91863-MS.

Perrin, C., Wani, M.R., Akbar, M., et al., 2007. Integration of borehole image log enhances conventional electrofacies analysis in dual porosity carbonate reservoirs. In: Presented at the SPE International Petroleum Technology Conference, Dubai, UAE, 4–6 December. IPTC-11622-MS. https://doi.org/10.2523/IPTC-11622-MS.

Pirrone, M., Bona, N., 2015. A novel approach for a fast and accurate petrophysical characterization of carbonate reservoirs based on NMR. In: Presented at the SPE Reservoir Characterization and Simulation Conference and Exhibition, Abu Dhabi, UAE, 14–16 September. SPE-175656-MS. https://doi.org/10.2118/175656-MS.

Ramakrishnan, T.S., Ramamoorthy, R., Fordham, E., et al., 2001. A model-based interpretation methodology for evaluating carbonate reservoirs. In: Presented at the SPE Annual Technical Conference and Exhibition, New Orleans, Louisiana, 30 September–3 October. SPE-71704-MS. https://doi.org/10.2118/71704-MS.

Ramamoorthy, R., Johnson, D.L., Murphy III, W.F., 1999. Porosity estimation method in carbonate rock. U.S. Patent No. 5, 869,755.

Ramamoorthy, R., Ramakrishnan, T.S., Dasgupta, S., et al., 2019. Towards a petrophysically consistent implementation of Archie's equation for heterogeneous carbonate rocks. In: Paper P Presented at the SPWLA 60th Annual Logging Symposium, Woodlands, Texas, 17–19 June. SPWLA-2019_P. https://doi.org/10.30632/T60ALS-2019_P.

Ramandi, H.L., Mostaghimi, P., Armstrong, R.T., 2017. Digital rock analysis for accurate prediction of fractured media permeability. J. Hydrol. 554 (November), 817–826 https://doi.org/10.1016/j.jhydrol.2016.08.029.

Raymer, L.L., Hunt, E.R., Gardner, J.S., 1980. An improved sonic transit time-to porosity transform. In: Paper P Presented at the SPWLA 21st Annual Logging Symposium, Lafayette, Louisiana, 8–11 July. SPWLA-1980-P.

Richa, R., Mukerji, T., Mavko, G., et al., 2006. Image analysis and pattern recognition for porosity estimation from thin sections. In: Presented at the SEG Annual Meeting (Technical Program), New Orleans, 1–6 October. SEG-2006-1968. https://doi.org/10.1190/1.2369918.

Rodolfo Soto, B., Cintia, M., Orlando, P., et al., 2012. A new reservoir classification based on pore types improves characterization. In: Presented at the Latin American and Carribbean Petroleum Engineering Conference, Mexico City, 16–18 April. SPE-152872-MS. https://doi.org/10.2118/152872-MS.

Sadeghnejad, S., Gostick, J., 2020. Multiscale reconstruction of vuggy carbonates by pore-network modeling and image-based technique. SPE J. 25 (1), 253–267. https://doi.org/10.2118/198902-PA. SPE-198902-PA.

Saneifar, M., Heidari, Z., Hill, A.D., 2015. Application of conventional well logs to characterize spatial heterogeneities in carbonate formations required for prediction of acid-fracture conductivity. SPE Prod. Oper. 30 (3), 243–256. https://doi.org/10.2118/173183-PA. SPE-173183-PA.

Salazar, M.J., Wang, G.L., Torres-Verdin, C., et al., 2008. Combined simulation and inversion of sp and resistivity logs for the estimation of connate-water resistivity and Archie's cementation exponent. Geophysics 73 (3), 107–114. https://doi.org/10.1190/1.2890408.

Saleh, A.A., Castagna, J.P., 2004. Revisiting the wyllie time average equation in the case of near-spherical pores. Geophysics 69 (1), 45–55. https://doi.org/10.1190/1.1649374.

Sayers, C.M., 2008. The elastic properties of carbonates. Lead. Edge 27 (8), 1020–1024. https://doi.org/10.1190/1.2967555.

Sajjad, G., Mehdi, D., Abdolhossein, A., 2016. Pore types distribution and their reservoir properties in the sequence stratigraphic framework: a case study from the Oligo-Miocene Asmari Formation, SW Iran. Arab J Geosci 9 (3), 194–213. https://doi.org/10.1007/s12517-015-2141-8.

Schlumberger, Inc, 1974. Log Interpretation Applications. Schlumberger Educational Service.

Schlumberger, Limited, 2009. Log Interpretation Charts, second ed. Sugar Land, Texas, USA https://www.slb.com/resources/publications/books/log_charts.aspx.

Serra, O., Abbott, H.T., 1982. The contribution of logging data to sedimentology and stratigraphy. SPE J. 22 (1), 117–131. https://doi.org/10.2118/9270-PA. SPE-9270–PA.

Smith, L.B., Eberli, G.P., Masaferro, J.L., et al., 2003. Discrimination of effective from ineffective porosity in heterogeneous cretaceous carbonates, Al-Ghubar field, Oman. AAPG Bull. 87 (9), 1509–1529.

Song, Z., Li, M., Zhao, C., et al., 2020. Gas injection for enhanced oil recovery in two-dimensional geology-based physical model of Tahe fractured-vuggy carbonate reservoirs: karst fault system. Petrol. Sci. 17, 419–433. https://doi.org/10.1007/s12182-020-00427-z.

Sun, H., Belhaj, H., Tao, G., et al., 2019. Rock properties evaluation for carbonate reservoir characterization with multi-scale digital rock images. J. Petrol. Sci. Eng. 175, 654–664. https://doi.org/10.1016/j.petrol.2018.12.075, 2019.

Sun, Y., 2000. Core-log-seismic integration in hemipelagic marine sediments on the eastern flank of the juan de fuca ridge. In: A Davis, E.E., Escutia, C. (Eds.),

Proceedings of the Ocean Drilling Program, Scientific Results, vol. 168, pp. 21–35, 2000.

Sun, Y., 2004. Effects of pore structure on elastic wave propagation in rocks, AVO modeling. J. Geophys. Eng. 1 (4), 268–276. https://doi.org/10.1088/1742-2132/1/4/005.

Sun, Y., Berteussen, K., Vega, S., et al., 2006. Effects of pore structure on 4D seismic signals in carbonate reservoirs. Presented at the SEG Annual Meeting (Technical Program) 25 (2), 3260–3264. https://doi.org/10.1190/1.2370208. SEG-2006-3260.

Tilke, P.G., Allen, D., Gyllensten, A., 2006. Quantitative analysis of porosity heterogeneity: application of geostatistics to borehole images. Math. Geol. 38 (2), 155–174. https://doi.org/10.1007/s11004-005-9011-y.

Tixier, M.P., Alger, R.P., 1970. Log evaluation of non-metallic mineral deposits. Geophysics 35 (1), 124–142. https://doi.org/10.1190/1.1440070.

Tonietto, S.N., Smoot, M.Z., Pope, M., 2014. Pore type characterization and classification in carbonate reservoirs. In: Presented at the AAPG Annual Convention and Exhibition, Houston, Texas, 6–9 April. Search and Discovery Article #41432.

Tyagi, A.K., Bhaduri, A., 2002. Porosity analysis using borehole electrical images in carbonate reservoirs. In: Paper KK Presented at the SPWLA 43rd Annual Logging Symposium, Oiso, Japan, 2–5 June. SPWLA-2002-KK.

Ukar, E., Baqués, V., Laubach, S.E., et al., 2020. The Nature and Origins of Decameter-Scale Porosity in Ordovician Carbonate Rocks, Halahatang Oilfield, Tarim Basin, China. Journal of the Geological Society. https://doi.org/10.6084/m9.figshare.c.4946046.v1. Accepted.

Valentín, M.B., Bom, C.R., Martins Compan, A.L., et al., 2018. Estimation of permeability and effective porosity logs using deep autoencoders in borehole image logs from the brazilian pre-salt carbonate. J. Petrol. Sci. Eng. 170, 315–330. https://doi.org/10.1016/j.petrol.2018.06.038, 2018.

Vik, B., Bastesen, E., Skauge, A., 2013. Evaluation of representative elementary volume for a vuggy carbonate rock—part: porosity, permeability, and dispersivity. J. Petrol. Sci. Eng. 112 (December), 36–47 https://dx.doi.org/10.1016/j.petrol.2013.03.029.

Voorn, M., Exner, U., Barnhoorn, A., et al., 2015. Porosity, permeability and 3D fracture network characterization of dolomite reservoir rock samples. J. Petrol. Sci. Eng. 127 (March), 270–285 https://dx.doi.org/10.1016/j.petrol.2014.12.019.

Wang, F., Li, Y., Tang, X., et al., 2016. Petrophysical properties analysis of a carbonate reservoir with natural fractures and vugs using X-ray computed tomography. J. Nat. Gas Sci. Eng. 28 (January), 215–225. https://doi.org/10.1016/j.jngse.2015.11.046.

Wang, F.P., Lucia, F.J., 1993. Comparison of empirical models for calculating the vuggy porosity and cementation exponent of carbonates from log responses. University of Texas, Bureau of Economic Geology. Geological Circular 93–4, 27.

Wang, H.Y., Sun, S.Z., Yang, H., et al., 2011. The influence of pore structure on p- & s-wave velocities in complex carbonate reservoirs with secondary storage space. Petrol. Sci. 8 (4), 394–405. https://doi.org/10.1007/s12182-011-0157-6.

Wardaya, P.D., Khairy, H., Sum, C.W., 2013. Integrating digital image processing and artificial neural network for estimating porosity from thin section. In: Presented at the International Petroleum Technology Conference, Beijing, 26–28 March. IPTC-16959-MS. https://doi.org/10.2523/IPTC-16959-MS.

Weger, R.J., Eberli, G.P., Baechle, G.T., et al., 2009. Quantification of pore structure and its effect on sonic velocity and permeability in carbonates. Geohorizons, AAPG Bull. 93 (10), 1297–1317. https://doi.org/10.1306/05270909001.

Wei, D., Gao, Z., Fan, T., et al., 2020. The rock-fabric/petrophysical characteristics and classification of the micropores hosted between the calcite and dolomite crystals, 2020 J. Petrol. Sci. Eng. 193, 107383. https://doi.org/10.1016/j.petrol.2020.107383, 1-13.

Winn, R.H., 1957. Log interpretation in heterogeneous carbonate reservoirs. SPE Pet Trans 210, 268–274. https://doi.org/10.2118/SPE-818-G. SPE-818-G.

Wyllie, M.R.J., Gregory, A.R., Gardner, L.W., 1956. Elastic wave velocities in heterogeneous and porous media. Geophysics 21 (1), 41–70. https://doi.org/10.1190/1.1438217.

Xu, C., Russell, D., Gournay, J., et al., 2006. Porosity partitioning and permeability quantification in vuggy carbonates using wireline logs, Permian Basin, West Texas. Petrophysics 47 (February), 13–22. SPWLA-2006-V47N1A1.

Xu, J., Zhang, B., Qin, Y., et al., 2016. Method for calculating the fracture porosity of tight-fracture reservoirs. Geophysics 81 (4), IM57–IM70. https://doi.org/10.1190/geo2015-0434.1.

Xu, S., Payne, M.A., 2009. Modeling elastic properties in carbonate rocks. Lead. Edge 28 (1), 66–74. https://doi.org/10.1190/1.3064148.

Yarmohammadi, S., Kadkhodaie, A., Hosseinzadeh, S., 2020. An integrated approach for heterogeneity analysis of carbonate reservoirs by using image log based porosity distributions, NMR T2 curves, velocity deviation log and petrographic studies: a case study from the South Pars gas field, Persian Gulf Basin, 2020 J. Petrol. Sci. Eng. 192, 107283. https://doi.org/10.1016/j.petrol.2020.107283, 1-12.

Yu, B.S., Chen, J.Q., Lin, C.S., 2001. Cambrian–ordovician sequence stratigraphy on the northern Tarim platform and its correlation with yantze platform and North China platform. SCIENCE IN CHNA (Series D) 44 (4), 373–384.

Yu, B.S., Ruan, Z., Zhang, C., et al., 2016. Tectonic evolution of Tarim Basin in cambrian–ordovician and its implication for reservoir development, NW China. J EARTH SYST SCI 125 (2), 285–300.

Zhu, D., Meng, Q., Jin, Z., et al., 2015. Formation mechanism of deep cambrian dolomite reservoirs in the Tarim Basin, Northwestern China. Mar. Petrol. Geol. 59 (January), 232–244. https://doi.org/10.1016/j.marpetgeo.2014.08.022.

Zohreh, M., Junin, R., Bakhtiary, H.A., et al., 2016. The Evaluation of borehole imaging result comparing with cores in Sarvak Fractured and Non-fractured Reservoir. Arab J Geosci 9 (3), 225–237. https://doi.org/10.1007/s12517-015-2091-1.